

# Nonperturbative-transverse-momentum effects and evolution in dihadron and direct photon-hadron angular correlations in $p+p$ collisions at $\sqrt{s}=510$ GeV

A. Adare,<sup>13</sup> C. Aidala,<sup>39,43</sup> N.N. Ajitanand,<sup>61</sup> Y. Akiba,<sup>56,57,\*</sup> R. Akimoto,<sup>12</sup> J. Alexander,<sup>61</sup> M. Alfred,<sup>24</sup> V. Andrieux,<sup>43</sup> K. Aoki,<sup>32,56</sup> N. Apadula,<sup>29,62</sup> Y. Aramaki,<sup>56</sup> H. Asano,<sup>35,56</sup> E.T. Atomssa,<sup>62</sup> T.C. Awes,<sup>52</sup> C. Ayuso,<sup>43</sup> B. Azmoun,<sup>7</sup> V. Babintsev,<sup>25</sup> M. Bai,<sup>6</sup> X. Bai,<sup>11</sup> N.S. Bandara,<sup>42</sup> B. Bannier,<sup>62</sup> K.N. Barish,<sup>8</sup> S. Bathe,<sup>5,57</sup> V. Baublis,<sup>55</sup> C. Baumann,<sup>7</sup> S. Baumgart,<sup>56</sup> A. Bazilevsky,<sup>7</sup> M. Beaumier,<sup>8</sup> S. Beckman,<sup>13</sup> R. Belmont,<sup>13,43,67</sup> A. Berdnikov,<sup>59</sup> Y. Berdnikov,<sup>59</sup> D. Black,<sup>8</sup> D.S. Blau,<sup>34</sup> M. Boer,<sup>39</sup> J.S. Bok,<sup>50</sup> K. Boyle,<sup>57</sup> M.L. Brooks,<sup>39</sup> J. Bryslawskij,<sup>5,8</sup> H. Buesching,<sup>7</sup> V. Bumazhnov,<sup>25</sup> C. Butler,<sup>21</sup> S. Butsyk,<sup>49</sup> S. Campbell,<sup>14,29</sup> V. Canoa Roman,<sup>62</sup> R. Cervantes,<sup>62</sup> C.-H. Chen,<sup>57</sup> C.Y. Chi,<sup>14</sup> M. Chiu,<sup>7</sup> I.J. Choi,<sup>26</sup> J.B. Choi,<sup>10,†</sup> S. Choi,<sup>60</sup> P. Christiansen,<sup>40</sup> T. Chujo,<sup>66</sup> V. Cianciolo,<sup>52</sup> Z. Citron,<sup>68</sup> B.A. Cole,<sup>14</sup> M. Connors,<sup>21,57</sup> N. Cronin,<sup>44,62</sup> N. Crossette,<sup>44</sup> M. Csanád,<sup>17</sup> T. Csörgő,<sup>18,69</sup> T.W. Danley,<sup>51</sup> A. Datta,<sup>49</sup> M.S. Daugherty,<sup>1</sup> G. David,<sup>7</sup> K. DeBlasio,<sup>49</sup> K. Dehmelt,<sup>62</sup> A. Denisov,<sup>25</sup> A. Deshpande,<sup>57,62</sup> E.J. Desmond,<sup>7</sup> L. Ding,<sup>29</sup> A. Dion,<sup>62</sup> D. Dixit,<sup>62</sup> J.H. Do,<sup>70</sup> L. D’Orazio,<sup>41</sup> O. Drapier,<sup>36</sup> A. Drees,<sup>62</sup> K.A. Drees,<sup>6</sup> M. Dumancic,<sup>68</sup> J.M. Durham,<sup>39</sup> A. Durum,<sup>25</sup> T. Elder,<sup>18,21</sup> T. Engelmore,<sup>14</sup> A. Enokizono,<sup>56,58</sup> H. En’yo,<sup>56,57</sup> S. Esumi,<sup>66</sup> K.O. Eyser,<sup>7</sup> B. Fadem,<sup>44</sup> W. Fan,<sup>62</sup> N. Feege,<sup>62</sup> D.E. Fields,<sup>49</sup> M. Finger,<sup>9</sup> M. Finger, Jr.,<sup>9</sup> F. Fleuret,<sup>36</sup> S.L. Fokin,<sup>34</sup> J.E. Frantz,<sup>51</sup> A. Franz,<sup>7</sup> A.D. Frawley,<sup>20</sup> Y. Fukao,<sup>32</sup> Y. Fukuda,<sup>66</sup> T. Fusayasu,<sup>46</sup> K. Gainey,<sup>1</sup> C. Gal,<sup>62</sup> P. Gallus,<sup>15</sup> P. Garg,<sup>3,62</sup> A. Garishvili,<sup>64</sup> I. Garishvili,<sup>38</sup> H. Ge,<sup>62</sup> F. Giordano,<sup>26</sup> A. Glenn,<sup>38</sup> X. Gong,<sup>61</sup> M. Gonin,<sup>36</sup> Y. Goto,<sup>56,57</sup> R. Granier de Cassagnac,<sup>36</sup> N. Grau,<sup>2</sup> S.V. Greene,<sup>67</sup> M. Grosse Perdekamp,<sup>26</sup> Y. Gu,<sup>61</sup> T. Gunji,<sup>12</sup> H. Guragain,<sup>21</sup> T. Hachiya,<sup>56,57</sup> J.S. Haggerty,<sup>7</sup> K.I. Hahn,<sup>19</sup> H. Hamagaki,<sup>12</sup> H.F. Hamilton,<sup>1</sup> S.Y. Han,<sup>19</sup> J. Hanks,<sup>62</sup> S. Hasegawa,<sup>30</sup> T.O.S. Haseler,<sup>21</sup> K. Hashimoto,<sup>56,58</sup> R. Hayano,<sup>12</sup> X. He,<sup>21</sup> T.K. Hemmick,<sup>62</sup> T. Hester,<sup>8</sup> J.C. Hill,<sup>29</sup> K. Hill,<sup>13</sup> R.S. Hollis,<sup>8</sup> K. Homma,<sup>23</sup> B. Hong,<sup>33</sup> T. Hoshino,<sup>23</sup> N. Hotvedt,<sup>29</sup> J. Huang,<sup>7,39</sup> S. Huang,<sup>67</sup> T. Ichihara,<sup>56,57</sup> Y. Ikeda,<sup>56</sup> K. Imai,<sup>30</sup> Y. Imazu,<sup>56</sup> J. Imrek,<sup>16</sup> M. Inaba,<sup>66</sup> A. Iordanova,<sup>8</sup> D. Isenhower,<sup>1</sup> A. Isinhue,<sup>44</sup> Y. Ito,<sup>47</sup> D. Ivanishchev,<sup>55</sup> B.V. Jacak,<sup>62</sup> S.J. Jeon,<sup>45</sup> M. Jezghani,<sup>21</sup> Z. Ji,<sup>62</sup> J. Jia,<sup>7,61</sup> X. Jiang,<sup>39</sup> B.M. Johnson,<sup>7,21</sup> E. Joo,<sup>33</sup> K.S. Joo,<sup>45</sup> V. Jorjadze,<sup>62</sup> D. Jouan,<sup>53</sup> D.S. Jumper,<sup>26</sup> J. Kamin,<sup>62</sup> S. Kanda,<sup>12,32,56</sup> B.H. Kang,<sup>22</sup> J.H. Kang,<sup>70</sup> J.S. Kang,<sup>22</sup> D. Kapukchyan,<sup>8</sup> J. Kapustinsky,<sup>39</sup> S. Karthas,<sup>62</sup> D. Kawall,<sup>42</sup> A.V. Kazantsev,<sup>34</sup> J.A. Key,<sup>49</sup> V. Khachatryan,<sup>62</sup> P.K. Khandai,<sup>3</sup> A. Khanzadeev,<sup>55</sup> K. Kihara,<sup>66</sup> K.M. Kijima,<sup>23</sup> C. Kim,<sup>8,33</sup> D.H. Kim,<sup>19</sup> D.J. Kim,<sup>31</sup> E.-J. Kim,<sup>10</sup> H.-J. Kim,<sup>70</sup> M. Kim,<sup>33,60</sup> Y.-J. Kim,<sup>26</sup> Y.K. Kim,<sup>22</sup> D. Kincses,<sup>17</sup> E. Kistenev,<sup>7</sup> J. Klatsky,<sup>20</sup> D. Kleinjan,<sup>8</sup> P. Kline,<sup>62</sup> T. Koblesky,<sup>13</sup> M. Kofarago,<sup>17,69</sup> B. Komkov,<sup>55</sup> J. Koster,<sup>57</sup> D. Kotchetkov,<sup>51</sup> D. Kotov,<sup>55,59</sup> F. Krizek,<sup>31</sup> S. Kudo,<sup>66</sup> K. Kurita,<sup>58</sup> M. Kurosawa,<sup>56,57</sup> Y. Kwon,<sup>70</sup> R. Lacey,<sup>61</sup> Y.S. Lai,<sup>14</sup> J.G. Lajoie,<sup>29</sup> E.O. Lallow,<sup>44</sup> A. Lebedev,<sup>29</sup> D.M. Lee,<sup>39</sup> G.H. Lee,<sup>10</sup> J. Lee,<sup>19,63</sup> K.B. Lee,<sup>39</sup> K.S. Lee,<sup>33</sup> S. Lee,<sup>70</sup> S.H. Lee,<sup>62</sup> M.J. Leitch,<sup>39</sup> M. Leitgab,<sup>26</sup> Y.H. Leung,<sup>62</sup> B. Lewis,<sup>62</sup> N.A. Lewis,<sup>43</sup> X. Li,<sup>11</sup> X. Li,<sup>39</sup> S.H. Lim,<sup>39,70</sup> L. D. Liu,<sup>54</sup> M.X. Liu,<sup>39</sup> V-R Loggins,<sup>26</sup> V.-R. Loggins,<sup>26</sup> K. Lovasz,<sup>16</sup> D. Lynch,<sup>7</sup> C.F. Maguire,<sup>67</sup> T. Majoros,<sup>16</sup> Y.I. Makdisi,<sup>6</sup> M. Makek,<sup>68,71</sup> M. Malaev,<sup>55</sup> A. Manion,<sup>62</sup> V.I. Manko,<sup>34</sup> E. Mannel,<sup>7</sup> H. Masuda,<sup>58</sup> M. McCumber,<sup>13,39</sup> P.L. McGaughey,<sup>39</sup> D. McGlinchey,<sup>13,20</sup> C. McKinney,<sup>26</sup> A. Meles,<sup>50</sup> M. Mendoza,<sup>8</sup> B. Meredith,<sup>14,26</sup> Y. Miake,<sup>66</sup> T. Mibe,<sup>32</sup> A.C. Mignerey,<sup>41</sup> D.E. Mihalik,<sup>62</sup> A.J. Miller,<sup>1</sup> A. Milov,<sup>68</sup> D.K. Mishra,<sup>4</sup> J.T. Mitchell,<sup>7</sup> G. Mitsuka,<sup>57</sup> S. Miyasaka,<sup>56,65</sup> S. Mizuno,<sup>56,66</sup> A.K. Mohanty,<sup>4</sup> S. Mohapatra,<sup>61</sup> P. Montuenga,<sup>26</sup> T. Moon,<sup>70</sup> D.P. Morrison,<sup>7</sup> S.I.M. Morrow,<sup>67</sup> M. Moskowitz,<sup>44</sup> T.V. Moukhanova,<sup>34</sup> T. Murakami,<sup>35,56</sup> J. Murata,<sup>56,58</sup> A. Mwai,<sup>61</sup> T. Nagae,<sup>35</sup> K. Nagai,<sup>65</sup> S. Nagamiya,<sup>32,56</sup> K. Nagashima,<sup>23</sup> T. Nagashima,<sup>58</sup> J.L. Nagle,<sup>13</sup> M.I. Nagy,<sup>17</sup> I. Nakagawa,<sup>56,57</sup> H. Nakagomi,<sup>56,66</sup> Y. Nakamiya,<sup>23</sup> K.R. Nakamura,<sup>35,56</sup> T. Nakamura,<sup>56</sup> K. Nakano,<sup>56,65</sup> C. Nattrass,<sup>64</sup> P.K. Netrakanti,<sup>4</sup> M. Nishida,<sup>23,56</sup> T. Niida,<sup>66</sup> R. Nouicer,<sup>7,57</sup> T. Novák,<sup>18,69</sup> N. Novitzky,<sup>31,62</sup> R. Novotny,<sup>15</sup> A.S. Nyanin,<sup>34</sup> E. O’Brien,<sup>7</sup> C.A. Ogilvie,<sup>29</sup> H. Oide,<sup>12</sup> K. Okada,<sup>57</sup> J.D. Orjuela Koop,<sup>13</sup> J.D. Osborn,<sup>43</sup> A. Oskarsson,<sup>40</sup> G.J. Ottino,<sup>49</sup> K. Ozawa,<sup>32,66</sup> R. Pak,<sup>7</sup> V. Pantuev,<sup>27</sup> V. Papavassiliou,<sup>50</sup> I.H. Park,<sup>19,63</sup> J.S. Park,<sup>60</sup> S. Park,<sup>56,60,62</sup> S.K. Park,<sup>33</sup> S.F. Pate,<sup>50</sup> L. Patel,<sup>21</sup> M. Patel,<sup>29</sup> J.-C. Peng,<sup>26</sup> W. Peng,<sup>67</sup> D.V. Perepelitsa,<sup>7,13,14</sup> G.D.N. Perera,<sup>50</sup> D.Yu. Peressounko,<sup>34</sup> C.E. PerezLara,<sup>62</sup> J. Perry,<sup>29</sup> R. Petti,<sup>7,62</sup> M. Phipps,<sup>7,26</sup> C. Pinkenburg,<sup>7</sup> R. Pinson,<sup>1</sup> R.P. Pisani,<sup>7</sup> A. Pun,<sup>51</sup> M.L. Purschke,<sup>7</sup> H. Qu,<sup>1</sup> J. Rak,<sup>31</sup> I. Ravinovich,<sup>68</sup> K.F. Read,<sup>52,64</sup> D. Reynolds,<sup>61</sup> V. Riabov,<sup>48,55</sup> Y. Riabov,<sup>55,59</sup> E. Richardson,<sup>41</sup> D. Richford,<sup>5</sup> T. Rinn,<sup>29</sup> N. Riveli,<sup>51</sup> D. Roach,<sup>67</sup> S.D. Rolnick,<sup>8</sup> M. Rosati,<sup>29</sup> Z. Rowan,<sup>5</sup> J.G. Rubin,<sup>43</sup> J. Runchey,<sup>29</sup> M.S. Ryu,<sup>22</sup> A.S. Safonov,<sup>59</sup> B. Sahlmuller,<sup>62</sup> N. Saito,<sup>32</sup> T. Sakaguchi,<sup>7</sup> H. Sako,<sup>30</sup> V. Samsonov,<sup>48,55</sup> M. Sarsour,<sup>21</sup> K. Sato,<sup>66</sup> S. Sato,<sup>30</sup> S. Sawada,<sup>32</sup> B. Schaefer,<sup>67</sup> B.K. Schmoll,<sup>64</sup> K. Sedgwick,<sup>8</sup> J. Seele,<sup>57</sup> R. Seidl,<sup>56,57</sup> Y. Sekiguchi,<sup>12</sup> A. Sen,<sup>21,29,64</sup> R. Seto,<sup>8</sup> P. Sett,<sup>4</sup> A. Sexton,<sup>41</sup> D. Sharma,<sup>62</sup> A. Shaver,<sup>29</sup> I. Shein,<sup>25</sup> T.-A. Shibata,<sup>56,65</sup> K. Shigaki,<sup>23</sup> M. Shimomura,<sup>29,47</sup> T. Shioya,<sup>66</sup> K. Shoji,<sup>56</sup> P. Shukla,<sup>4</sup> A. Sickles,<sup>7,26</sup> C.L. Silva,<sup>39</sup> D. Silvermyr,<sup>40,52</sup> B.K. Singh,<sup>3</sup> C.P. Singh,<sup>3</sup> V. Singh,<sup>3</sup> M. Skolnik,<sup>44</sup> M. Slunečka,<sup>9</sup>

K.L. Smith,<sup>20</sup> M. Snowball,<sup>39</sup> S. Solano,<sup>44</sup> R.A. Soltz,<sup>38</sup> W.E. Sondheim,<sup>39</sup> S.P. Sorensen,<sup>64</sup> I.V. Sourikova,<sup>7</sup>  
 P.W. Stankus,<sup>52</sup> P. Steinberg,<sup>7</sup> E. Stenlund,<sup>40</sup> M. Stepanov,<sup>42,†</sup> A. Ster,<sup>69</sup> S.P. Stoll,<sup>7</sup> M.R. Stone,<sup>13</sup>  
 T. Sugitate,<sup>23</sup> A. Sukhanov,<sup>7</sup> T. Sumita,<sup>56</sup> J. Sun,<sup>62</sup> S. Syed,<sup>21</sup> J. Sziklai,<sup>69</sup> A. Takahara,<sup>12</sup> A. Takeda,<sup>47</sup>  
 A. Taketani,<sup>56,57</sup> Y. Tanaka,<sup>46</sup> K. Tanida,<sup>30,57,60</sup> M.J. Tannenbaum,<sup>7</sup> S. Tarafdar,<sup>3,67,68</sup> A. Taranenko,<sup>48,61</sup>  
 G. Tarnai,<sup>16</sup> E. Tennant,<sup>50</sup> R. Tieulent,<sup>21</sup> A. Timilsina,<sup>29</sup> T. Todoroki,<sup>56,66</sup> M. Tomášek,<sup>15,28</sup> H. Torii,<sup>12</sup>  
 C.L. Towell,<sup>1</sup> M. Towell,<sup>1</sup> R. Towell,<sup>1</sup> R.S. Towell,<sup>1</sup> I. Tserriya,<sup>68</sup> Y. Ueda,<sup>23</sup> B. Ujvari,<sup>16</sup> H.W. van Hecke,<sup>39</sup>  
 M. Vargyas,<sup>17,69</sup> S. Vazquez-Carson,<sup>13</sup> E. Vazquez-Zambrano,<sup>14</sup> A. Veicht,<sup>14</sup> J. Velkovska,<sup>67</sup> R. Vértesi,<sup>69</sup>  
 M. Virius,<sup>15</sup> V. Vrba,<sup>15,28</sup> N. Vukman,<sup>71</sup> E. Vznuzdaev,<sup>55</sup> X.R. Wang,<sup>50,57</sup> Z. Wang,<sup>5</sup> D. Watanabe,<sup>23</sup>  
 K. Watanabe,<sup>56,58</sup> Y. Watanabe,<sup>56,57</sup> Y.S. Watanabe,<sup>12,32</sup> F. Wei,<sup>50</sup> S. Whitaker,<sup>29</sup> S. Wolin,<sup>26</sup> C.P. Wong,<sup>21</sup>  
 C.L. Woody,<sup>7</sup> M. Wysocki,<sup>52</sup> B. Xia,<sup>51</sup> C. Xu,<sup>50</sup> Q. Xu,<sup>67</sup> L. Xue,<sup>21</sup> S. Yalcin,<sup>62</sup> Y.L. Yamaguchi,<sup>12,57,62</sup>  
 H. Yamamoto,<sup>66</sup> A. Yanovich,<sup>25</sup> P. Yin,<sup>13</sup> S. Yokkaichi,<sup>56,57</sup> J.H. Yoo,<sup>33</sup> I. Yoon,<sup>60</sup> Z. You,<sup>39</sup> I. Younus,<sup>37,49</sup>  
 H. Yu,<sup>50,54</sup> I.E. Yushmanov,<sup>34</sup> W.A. Zajc,<sup>14</sup> A. Zelenski,<sup>6</sup> S. Zharko,<sup>59</sup> S. Zhou,<sup>11</sup> and L. Zou<sup>8</sup>

(PHENIX Collaboration)

<sup>1</sup>Abilene Christian University, Abilene, Texas 79699, USA

<sup>2</sup>Department of Physics, Augustana University, Sioux Falls, South Dakota 57197, USA

<sup>3</sup>Department of Physics, Banaras Hindu University, Varanasi 221005, India

<sup>4</sup>Bhabha Atomic Research Centre, Bombay 400 085, India

<sup>5</sup>Baruch College, City University of New York, New York, New York, 10010 USA

<sup>6</sup>Collider-Accelerator Department, Brookhaven National Laboratory, Upton, New York 11973-5000, USA

<sup>7</sup>Physics Department, Brookhaven National Laboratory, Upton, New York 11973-5000, USA

<sup>8</sup>University of California-Riverside, Riverside, California 92521, USA

<sup>9</sup>Charles University, Ovocný trh 5, Praha 1, 116 36, Prague, Czech Republic

<sup>10</sup>Chonbuk National University, Jeonju, 561-756, Korea

<sup>11</sup>Science and Technology on Nuclear Data Laboratory, China Institute of Atomic Energy, Beijing 102413, People's Republic of China

<sup>12</sup>Center for Nuclear Study, Graduate School of Science, University of Tokyo, 7-3-1 Hongo, Bunkyo, Tokyo 113-0033, Japan

<sup>13</sup>University of Colorado, Boulder, Colorado 80309, USA

<sup>14</sup>Columbia University, New York, New York 10027 and Nevis Laboratories, Irvington, New York 10533, USA

<sup>15</sup>Czech Technical University, Zikova 4, 166 36 Prague 6, Czech Republic

<sup>16</sup>Debrecen University, H-4010 Debrecen, Egyetem tér 1, Hungary

<sup>17</sup>ELTE, Eötvös Loránd University, H-1117 Budapest, Pázmány P. s. 1/A, Hungary

<sup>18</sup>Eszterházy Károly University, Károly Róbert Campus, H-3200 Gyöngyös, Mátrai út 36, Hungary

<sup>19</sup>Ewha Womans University, Seoul 120-750, Korea

<sup>20</sup>Florida State University, Tallahassee, Florida 32306, USA

<sup>21</sup>Georgia State University, Atlanta, Georgia 30303, USA

<sup>22</sup>Hanyang University, Seoul 133-792, Korea

<sup>23</sup>Hiroshima University, Kagamiyama, Higashi-Hiroshima 739-8526, Japan

<sup>24</sup>Department of Physics and Astronomy, Howard University, Washington, DC 20059, USA

<sup>25</sup>IHEP Protvino, State Research Center of Russian Federation, Institute for High Energy Physics, Protvino, 142281, Russia

<sup>26</sup>University of Illinois at Urbana-Champaign, Urbana, Illinois 61801, USA

<sup>27</sup>Institute for Nuclear Research of the Russian Academy of Sciences, prospekt 60-letiya Oktyabrya 7a, Moscow 117312, Russia

<sup>28</sup>Institute of Physics, Academy of Sciences of the Czech Republic, Na Slovance 2, 182 21 Prague 8, Czech Republic

<sup>29</sup>Iowa State University, Ames, Iowa 50011, USA

<sup>30</sup>Advanced Science Research Center, Japan Atomic Energy Agency, 2-4

Shirakata Shirane, Tokai-mura, Naka-gun, Ibaraki-ken 319-1195, Japan

<sup>31</sup>Helsinki Institute of Physics and University of Jyväskylä, P.O.Box 35, FI-40014 Jyväskylä, Finland

<sup>32</sup>KEK, High Energy Accelerator Research Organization, Tsukuba, Ibaraki 305-0801, Japan

<sup>33</sup>Korea University, Seoul, 136-701, Korea

<sup>34</sup>National Research Center "Kurchatov Institute", Moscow, 123098 Russia

<sup>35</sup>Kyoto University, Kyoto 606-8502, Japan

<sup>36</sup>Laboratoire Leprince-Ringuet, Ecole Polytechnique, CNRS-IN2P3, Route de Saclay, F-91128, Palaiseau, France

<sup>37</sup>Physics Department, Lahore University of Management Sciences, Lahore 54792, Pakistan

<sup>38</sup>Lawrence Livermore National Laboratory, Livermore, California 94550, USA

<sup>39</sup>Los Alamos National Laboratory, Los Alamos, New Mexico 87545, USA

<sup>40</sup>Department of Physics, Lund University, Box 118, SE-221 00 Lund, Sweden

<sup>41</sup>University of Maryland, College Park, Maryland 20742, USA

<sup>42</sup>Department of Physics, University of Massachusetts, Amherst, Massachusetts 01003-9337, USA

<sup>43</sup>Department of Physics, University of Michigan, Ann Arbor, Michigan 48109-1040, USA

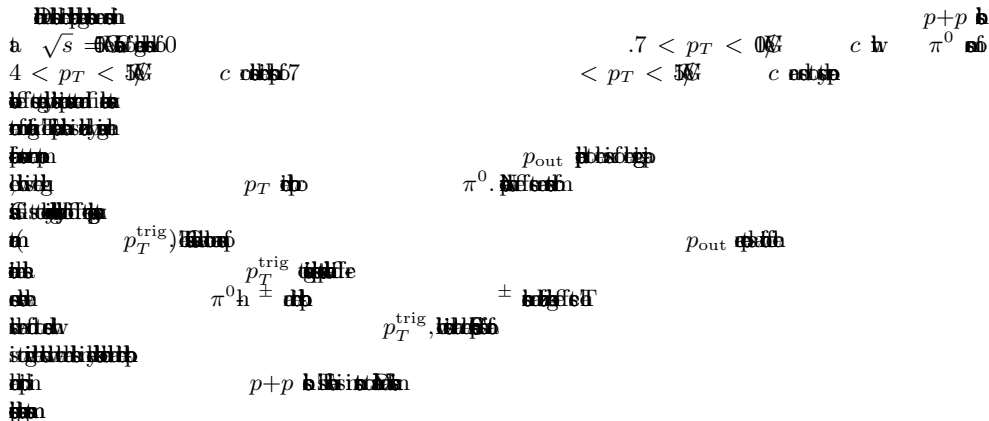
<sup>44</sup>Muhlenberg College, Allentown, Pennsylvania 18104-5586, USA

<sup>45</sup>Myongji University, Yongin, Kyonggido 449-728, Korea

<sup>46</sup>Nagasaki Institute of Applied Science, Nagasaki-shi, Nagasaki 851-0193, Japan

- <sup>47</sup> Nara Women's University, Kita-uoya Nishi-machi Nara 630-8506, Japan
- <sup>48</sup> National Research Nuclear University, MEPhI, Moscow Engineering Physics Institute, Moscow, 115409, Russia
- <sup>49</sup> University of New Mexico, Albuquerque, New Mexico 87131, USA
- <sup>50</sup> New Mexico State University, Las Cruces, New Mexico 88003, USA
- <sup>51</sup> Department of Physics and Astronomy, Ohio University, Athens, Ohio 45701, USA
- <sup>52</sup> Oak Ridge National Laboratory, Oak Ridge, Tennessee 37831, USA
- <sup>53</sup> IPN-Orsay, Univ. Paris-Sud, CNRS/IN2P3, Université Paris-Saclay, BP1, F-91406, Orsay, France
- <sup>54</sup> Peking University, Beijing 100871, People's Republic of China
- <sup>55</sup> PNPI, Petersburg Nuclear Physics Institute, Gatchina, Leningrad region, 188300, Russia
- <sup>56</sup> RIKEN Nishina Center for Accelerator-Based Science, Wako, Saitama 351-0198, Japan
- <sup>57</sup> RIKEN BNL Research Center, Brookhaven National Laboratory, Upton, New York 11973-5000, USA
- <sup>58</sup> Physics Department, Rikkyo University, 3-34-1 Nishi-Ikebukuro, Toshima, Tokyo 171-8501, Japan
- <sup>59</sup> Saint Petersburg State Polytechnic University, St. Petersburg, 195251 Russia
- <sup>60</sup> Department of Physics and Astronomy, Seoul National University, Seoul 151-742, Korea
- <sup>61</sup> Chemistry Department, Stony Brook University, SUNY, Stony Brook, New York 11794-3400, USA
- <sup>62</sup> Department of Physics and Astronomy, Stony Brook University, SUNY, Stony Brook, New York 11794-3800, USA
- <sup>63</sup> Sungkyunkwan University, Suwon, 440-746, Korea
- <sup>64</sup> University of Tennessee, Knoxville, Tennessee 37996, USA
- <sup>65</sup> Department of Physics, Tokyo Institute of Technology, Oh-okayama, Meguro, Tokyo 152-8551, Japan
- <sup>66</sup> Center for Integrated Research in Fundamental Science and Engineering, University of Tsukuba, Tsukuba, Ibaraki 305, Japan
- <sup>67</sup> Vanderbilt University, Nashville, Tennessee 37235, USA
- <sup>68</sup> Weizmann Institute, Rehovot 76100, Israel
- <sup>69</sup> Institute for Particle and Nuclear Physics, Wigner Research Centre for Physics, Hungarian Academy of Sciences (Wigner RCP, RMKI) H-1525 Budapest 114, POBox 49, Budapest, Hungary
- <sup>70</sup> Yonsei University, IPAP, Seoul 120-749, Korea
- <sup>71</sup> University of Zagreb, Faculty of Science, Department of Physics, Bijenička 32, HR-10002 Zagreb, Croatia

0000



PACS numbers: 25.75.Dw

## I. INTRODUCTION

In the last two decades, the study of quantum chromodynamics (QCD) bound states has evolved from static, one-dimensional snapshots of quarks and gluons to focus on multidimensional structure and the dynamics of partons. The theoretical framework that has been developed to describe parton dynamics in hadrons involves transverse-momentum-dependent (TMD) parton distribution functions (PDFs) and fragmentation functions (FFs). In traditional collinear PDFs and FFs, any momentum of the partons transverse to the hadron boost

axis is integrated over. In TMD PDFs or FFs, the transverse momentum of the partons is not integrated out and instead remains explicit in the PDF or FF, offering a means of describing the transverse momentum distribution of unpolarized partons within an unpolarized hadron, as well as a variety of spin-momentum correlations when polarized hadrons and/or partons are considered.

Early theoretical work in TMD PDFs took place in the 1980s by Collins, Soper, and Sterman [1–3], with extensive further development in the 1990s (see e.g. [4–6]). However, some theoretical details regarding the definition of TMD PDFs within a perturbative QCD (pQCD) framework have only been clarified in the last five years [7]. We note that due to confinement, the behavior of partons within hadrons is nonperturbative in

\* PHENIX Spokesperson: akiba@rcf.rhic.bnl.gov

† Deceased

that it cannot be calculated theoretically within pQCD. Collinear or TMD PDFs are nonperturbative functions that can be constrained by and/or used to predict high-energy scattering processes within a pQCD framework. In such a framework, the nonperturbative functions such as PDFs as well as FFs factorize from the perturbatively calculable partonic hard scattering cross section and from each other. Lattice QCD offers an alternative, complementary approach to pQCD, performing numerical nonperturbative calculations directly. In the past lattice QCD could only calculate moments of PDFs, integrated over parton collinear momentum fraction  $x$  as well as parton transverse momentum. However, recent developments have demonstrated the potential to go beyond these limitations. These efforts are still in very early stages [8–10].

There is already experimental evidence from semi-inclusive deep-inelastic scattering (SIDIS) and Drell-Yan (DY) measurements that several TMD PDFs describing spin-momentum correlations are nonzero [11–18]. In addition, there is empirical evidence for nonzero spin-momentum correlations in the process of hadronization from electron-positron annihilation as well as SIDIS [12, 17, 19–21]. Furthermore, transverse single-spin asymmetries up to  $\sim 40\%$  have been measured in inclusive hadron production in hadronic collisions, indicating large nonperturbative spin-momentum correlations in these processes (see e.g. [22–24]). However, these measurements cannot probe TMD functions directly because there is no simultaneous observation of perturbative and nonperturbative momentum scales.

The recent focus on multidimensional structure and parton dynamics has not only offered richer information on the behavior of partons confined within hadrons, but has moreover brought to light fundamental predictions regarding QCD as a nonAbelian gauge-invariant quantum field theory. In particular, the role of color interactions due to soft gluon exchanges with the remnants of the hard scattering have become clearer. Because TMD functions preserve more nonperturbative information compared to collinear functions, TMD functions can differ from collinear ones with regards to universality and factorization. For example, the Sivers TMD PDF [4], a correlation between the proton spin and quark transverse momentum, was shown to possibly be nonzero due to phase interference effects from soft gluon exchanges in SIDIS [25, 26]. Shortly afterward, Ref. [27] showed that, due to the gauge invariant nature of QCD and the parity and time (PT) odd nature of the Sivers TMD PDF, the function should be the same magnitude but opposite in sign when measured in Drell-Yan vs. SIDIS processes because of the different color flows possible in the initial state vs. final state. Twist-2 TMD PDFs that involve one polarization vector are odd under PT transformations, leading to this predicted effect. The nonvanishing nature of the Sivers function has already been measured in polarized SIDIS [11]; there is not yet a measurement of this function in polarized Drell-Yan. A first indication

from the Drell-Yan like W boson production exists [16]. The results favor a sign-change if TMD evolution effects are small, but at this stage the error bars are still large enough that a definitive statement can not be drawn from this single measurement. It is only for the TMD PDFs odd under PT transformations, where such sign-change behavior is expected, that gluon exchanges cannot be completely eliminated via a gauge transformation.

In the more complicated QCD process  $p+p$  to hadrons, soft gluon exchanges in both the initial and final state are possible, leading to new predicted effects for observables sensitive to a small transverse momentum scale. In such processes, factorization breaking has been predicted [28–31] in both polarized and unpolarized interactions. Here the nonperturbative objects in the cross section become correlated with one another and cannot be factorized into a convolution of TMD PDFs or TMD FFs. However, there are no theoretical claims that the perturbative partonic cross section does not factorize from the nonperturbative physics. Similarly to the case of the TMD PDFs that are odd under PT transformations, gluon exchanges that lead to the predicted factorization breaking cannot be eliminated via a gauge transformation. It is important to recognize that the ideas behind the predicted sign change of certain TMD PDFs and factorization breaking represent a major qualitative departure from previous purely perturbative approaches that do not account for soft gluon exchanges with remnants of the hard scattering. Possibly related effects known as “color coherence” have been studied and observed in multijet states in hadronic collisions [32–34], but these types of effects have not been rigorously treated in a TMD framework.

In calculations of TMD processes where factorization is predicted to hold, the evolution with the hard scale of the interaction is known to be governed by the Collins-Soper (CS) evolution equation [1, 2]. Note that the CS evolution equation comes directly out of the derivation of TMD factorization [35]. In contrast to the DGLAP collinear evolution equations [36–38], which are purely perturbative, the kernel for the CS evolution equation for TMD processes involves the Collins-Soper-Sterman (CSS) soft factor [3], which generally contains nonperturbative contributions. The soft factor is understood to be strongly universal, the same for unpolarized and polarized processes, PDFs and FFs, with the only difference being between quarks and gluons [39]. Because lattice calculations of the soft factor are currently not possible, the soft factor must be extracted from parameterizations of experimental measurements within a pQCD framework. For a discussion of the CSS soft factor and TMD evolution phenomenology, see Ref. [39].

The theoretical expectation from CSS evolution is that any momentum width sensitive to nonperturbative  $k_T$  would grow as the hard scale increases. This can be understood intuitively as a broadening of the phase space for gluon radiation with increasing hard scale. In addition this has been studied and observed in multiple phenomenological analyses of Drell-Yan and Z boson

data (see e.g. [40–42]), as well as phenomenological analyses of SIDIS data, where factorization is also predicted to hold (see e.g. [42–44]). As mentioned above, because the CS evolution equation comes directly out of the derivation of TMD factorization, it then follows that a promising avenue to investigate factorization breaking effects is by looking for qualitative differences from CSS evolution in processes where factorization breaking is expected, such as nearly back-to-back dihadron correlations produced in  $p+p$  collisions.

To have sensitivity to possible factorization breaking and modified TMD evolution effects, a particular observable must be sensitive to a small scale on the order of  $\Lambda_{QCD}$  and measured over a range of hard scales. Nearly back-to-back dihadron production has long been used as a proxy for measuring initial-state partonic transverse momentum  $k_T$  [45–48], which is defined in Fig. 1. First used in predictions by Ref. [49] as a method for understanding large differences in hard scattering cross sections between theory and data, nearly back-to-back two-particle and dijet angular correlations have since been used to measure  $k_T$  over a large range of center of mass energies [45, 47, 50, 51]. Direct photon-hadron correlations are of particular interest because the photon comes directly from the partonic hard scattering, and thus carries initial-state information without any final-state fragmentation effects. The direct photon approximates the away-side jet energy at leading order (LO) while still being directly sensitive to the partonic transverse momentum scale. Direct photons also give an interesting comparison to dihadron production because they do not carry color charge, thus, assuming factorization holds, only two TMD PDFs and one TMD FF are necessary in the cross section calculation compared to two TMD PDFs and two TMD FFs in dihadron production. Therefore, there should be more avenues for gluon exchange in nearly back-to-back dihadron events when compared to direct photon-hadron events.

Figure 1 shows the hard scattering kinematics of a nearly back-to-back dihadron event in the transverse plane. The effect of initial-state  $k_T$  and final-state  $j_T$ , the transverse momentum of the hadron with respect to the jet axis, can be probed in hadronic collisions by measuring the out-of-plane momentum component  $p_{\text{out}}$  with respect to the near-side hadron or direct photon, collectively referred to as the trigger particle.  $p_{\text{out}}$  thus quantifies the acoplanarity of the two-particle pair, with  $p_{\text{out}} = 0$  signifying exactly back-to-back particle production. Using the trigger particle as a proxy for the jet, the 1-dimensional quantity  $p_{\text{out}}$  is transverse to the  $p_T$  of the trigger particle,  $p_T^{\text{trig}}$ , and has a magnitude of:

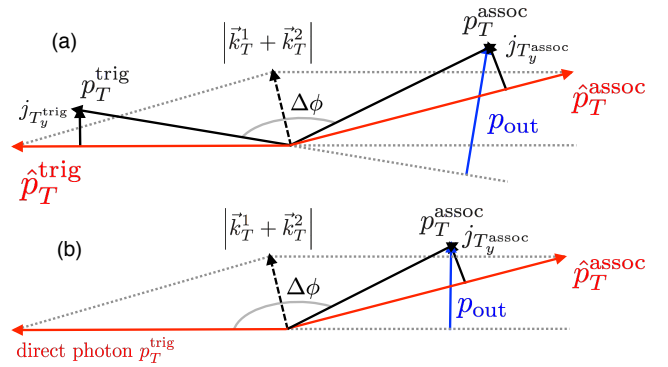
$$p_{\text{out}} = p_T^{\text{assoc}} \sin \Delta\phi \quad (1)$$

where  $p_T^{\text{assoc}}$  is the  $p_T$  of the associated hadron and  $\Delta\phi$  is the azimuthal angular separation between the trigger and associated particle as shown in Fig. 1. Reference [45] has shown that the root mean square of  $p_{\text{out}}$  and  $k_T$  are

related by

$$\frac{\langle z_T \rangle \sqrt{\langle k_T^2 \rangle}}{\hat{x}_h} = \frac{1}{x_h} \sqrt{\langle p_{\text{out}}^2 \rangle - \langle j_{T_y}^2 \rangle (1 + x_h^2)} \quad (2)$$

where  $\langle z_T \rangle = p_T^{\text{trig}} / \hat{p}_T^{\text{trig}}$  and  $x_h = \langle p_T^{\text{assoc}} \rangle / \langle p_T^{\text{trig}} \rangle$ , and quantities with a hat indicate partonic-level quantities. Note that in the determination of Eq. 2, it was assumed in Ref. [45] that the component  $j_{T_y}$  for both the trigger and associated jet axes was sampled from the same Gaussian distribution of  $\sqrt{\langle j_T^2 \rangle}$ . All the quantities on the left side of Eq. 2 are partonic, while those on the right side can be measured via the correlated away-side hadron. Equation 2 gives a clear definition for how to relate the root mean square initial-state  $k_T$  and final-state  $j_T$  to the observable  $p_{\text{out}}$ .



$$\sqrt{\langle k_T^2 \rangle} = \sqrt{\langle j_T^2 \rangle} = \sqrt{\langle j_{T_y}^2 \rangle} = \sqrt{\langle j_{T_y}^{\text{trig}2} \rangle} = \sqrt{\langle j_{T_y}^{\text{assoc}2} \rangle} = \sqrt{\langle p_{\text{out}}^2 \rangle} = \sqrt{\langle p_{\text{out}}^{\text{trig}2} \rangle} = \sqrt{\langle p_{\text{out}}^{\text{assoc}2} \rangle}$$

The Relativistic Heavy Ion Collider (RHIC) is an ideal facility to study nonperturbative factorization breaking effects because they are only predicted in hadronic collisions where at least one final-state hadron is measured, and the measurement has sensitivity to a small initial- and final-state transverse momentum scale. Observables of interest are final states where at least one particle has a large  $p_T$ , defining a hard scale, at least one final-state hadron is measured, and the observable is also sensitive to initial- and final-state  $k_T$  and  $j_T$ . At RHIC energies, the  $p_T$  reach for direct photons and pions is sufficiently large to have separation from the nonperturbative momentum

scale. Direct photon-hadron and  $\pi^0$ -hadron correlations were chosen specifically because of experimental capabilities and because of the differing number of final-state hadrons in the event; the  $\pi^0$ -hadron correlations probe an extra nonperturbative function, assuming factorization, and thus one more Gaussian  $j_T$  convolution than the direct photon-hadron correlations.

## II. EXPERIMENT DETAILS

In 2012 and 2013 the PHENIX experiment collected data from  $p+p$  collisions at  $\sqrt{s} = 510$  GeV. After data quality and vertex cuts, integrated luminosities of approximately  $30 \text{ pb}^{-1}$  in 2012 and  $152 \text{ pb}^{-1}$  in 2013 were used for the analysis of dihadron and direct photon-hadron correlated pairs. The measured  $p_{\text{out}}$  distributions presented here are at a higher center of mass energy and have significantly reduced statistical uncertainties compared to [50]. The higher center of mass energy also allows the probing of smaller  $x$  values of the TMD PDFs. Additionally, because the focus of this work is identifying possible nonperturbative factorization breaking effects, one of the observables presented here specifically isolates effects from nonperturbative  $k_T$  and  $j_T$ , extending previous measurements which only observed effects sensitive to both perturbative and nonperturbative contributions.

The PHENIX detector can measure two-particle correlations between photons and hadrons with its electromagnetic calorimeter (EMCal) and drift chamber (DC) plus pad chamber (PC) tracking system located in two central arms. The central arms are nearly back-to-back in azimuth, with each arm covering approximately  $\pi/2$  radians in azimuthal angle and 0.7 units of pseudorapidity about midrapidity [52]. A schematic showing the two central arms is shown in Fig. 2.

The EMCal [53] is located at a radial distance of approximately 5 meters from the beam pipe and is composed of 8 sectors, 4 in each arm. Six sectors are lead-scintillator (PbSc) sampling calorimeters, and the other two are lead glass (PbGl) Čerenkov calorimeters. The PbSc and PbGl calorimeters measure electromagnetic showers with intrinsic resolution  $\sigma_E/E = 2.1\% \oplus 8.1\%/\sqrt{E}$  and  $0.8\% \oplus 5.9\%/\sqrt{E}$ , respectively. High energy photons are identified with a cluster shower shape cut and charged particle veto. The shower shape cut also removes most high energy photons that overlap too closely with another photon, which helps eliminate  $\pi^0$  merging effects at energies greater than  $\sim 12$  GeV in the PbSc and  $\sim 17$  GeV in the PbGl. The granularity of the EMCal is  $\Delta\eta \times \Delta\phi \sim 0.011 \times 0.011$  for PbSc and  $0.008 \times 0.008$  for PbGl, where  $\Delta\eta$  and  $\Delta\phi$  refer to the pseudorapidity and azimuthal angular segmentation, respectively. The high granularity of the EMCal along with the shower shape cut allows for  $\pi^0$  and  $\eta$  reconstruction via the diphoton channel up to  $p_T \sim 17$  GeV. Previous direct-photon,  $\eta$ , and  $\pi^0$  cross sections measured in the PHENIX central arm can be found in [54–56].

The  $\pi^0$  and  $\eta$  mesons are tagged in the EMCal via their two-photon decay for the purposes of removing decay photon background to identify direct photons and constructing the  $\pi^0$ - $h^\pm$  correlated pairs. To reduce the combinatorial background, only photons with energy greater than 1 GeV are considered. The invariant mass windows were 120–160 MeV/ $c^2$  for  $\pi^0$  and 500–600 MeV/ $c^2$  for  $\eta$  mesons.

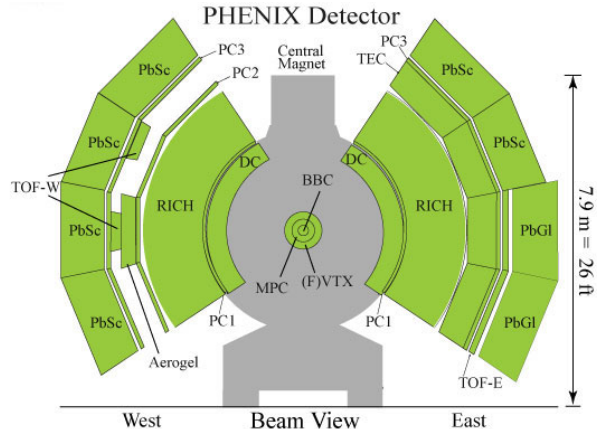


FIG. 2. Schematic of the PHENIX detector showing the West and East arms. The detector is 7.9 m = 26 ft high. The West arm contains TOF-W, Aerogel, and PbSc calorimeters. The East arm contains TOF-E, PbGl calorimeters, and PbSc calorimeters. The central magnet and BBC are located in the center. The tracking system consists of DC, PC, and PC3 detectors.

The PHENIX tracking system [57] allows charged hadron detection via a drift chamber (DC) in each central arm along with two pad chambers (PC) directly behind the drift chambers. The momentum resolution was determined to be  $\delta p/p = 0.7\% \oplus 1.0\%p$  with  $p$  in GeV/ $c$ . Tracks are identified via the DC, covering a radial distance of  $2.02 < r < 2.49$  meters from the beam pipe. Secondary tracks from decays or conversions are reduced by a condition that matches tracks in the DC to hits in the outermost PC3, located at a radial distance of 4.98 meters from the beam pipe. The charged particle veto suppresses hadronic showers in the EMCal by matching tracks from the full tracking system to clusters in the EMCal.

## III. CORRELATION FUNCTIONS

The correlation functions are constructed following the methods of Refs. [45, 46, 50]. The number of correlated hadrons per trigger particle is referred to as the per trigger yield, and is collected for the different types of trigger particle-associated hadron pairs. To quantify the inefficiencies of the PHENIX detector, the hadron yields are corrected by a charged hadron efficiency determined from a Monte Carlo single-particle generator and a GEANT-based simulation of the detector. Additionally, due to the limited acceptance of the PHENIX detector, the per-trigger yields are divided by a mixed event distribution.

Mixed event distributions are collected on a run-by-run basis to quantify any changing inefficiencies with time in the acceptance. The collected trigger particle is mixed with charged hadrons from different events and a mixed event correlation function is constructed to correct for the acceptance of the detector. In total the full correlation function is determined by the following equation

$$\frac{1}{N_{\text{trig}}} \frac{dN}{d\Delta\phi} = \frac{1}{N_{\text{trig}}} \frac{dN/d\Delta\phi_{\text{raw}}}{dN/d\Delta\phi_{\text{mixed}}\epsilon(p_T)} \quad (3)$$

where  $\epsilon(p_T)$  is the hadron efficiency described above. Note that this definition is general for any observable that could be constructed in a two-particle correlation, so it applies to the determination of the  $p_{\text{out}}$  distributions also. For a complete description of two-particle correlation analyses in the PHENIX central arms, see Refs. [45, 46, 50, 58].

### A. Statistical Subtraction of Decay Photons

To identify direct photons, Ref. [58] used a method that is based upon identifying a total sample of inclusive per-trigger yield correlations, then subtracting the decay component. From Ref. [58], the yield of charged hadrons per direct photon was determined with the following equation

$$Y_{\text{direct}} = \frac{1}{R_\gamma - 1} (R_\gamma Y_{\text{inclusive}} - Y_{\text{decay}}) \quad (4)$$

Here  $Y$  is the per-trigger yield where the trigger particle for each per-trigger yield is indicated as direct, inclusive, or decay, and  $R_\gamma$  is the relative contribution of direct photons to decay photons such that  $R_\gamma = N_{\text{inclusive}}/N_{\text{decay}}$ . The total yield of photons, the inclusive photons, comes from adding all of the decay and direct photons,  $N_{\text{inclusive}} = N_{\text{direct}} + N_{\text{decay}}$ . In Ref. [58] direct photons are defined as any photon not from a decay process, which includes next-to-leading order (NLO) photons that emerge from parton-to-photon fragmentation.

To eliminate the presence of NLO fragmentation photons, Ref. [50] implemented isolation and tagging cuts; thus Eq. 4 was modified to include these cuts. To determine the per-trigger yield of isolated direct photons, the number of isolated decay photons was subtracted from the isolated inclusive photon sample, where  $N_{\text{inclusive}}^{\text{iso}} = N_{\text{decay}}^{\text{iso}} + N_{\text{direct}}^{\text{iso}}$ . The subtraction procedure results in the following equation for per-trigger yields of isolated photon quantities [50]

$$Y_{\text{direct}}^{\text{iso}} = \frac{1}{R_\gamma^{\text{iso}} - 1} (R_\gamma^{\text{iso}} Y_{\text{inclusive}}^{\text{iso}} - Y_{\text{decay}}^{\text{iso}}) \quad (5)$$

where the trigger particles are noted as direct, inclusive, or decay for a given per-trigger yield  $Y$  and “iso”

refers to “isolated”.  $R_\gamma^{\text{iso}}$  is the relative contribution of isolated direct and decay photons, where  $R_\gamma^{\text{iso}} = N_{\text{inclusive}}^{\text{iso}}/N_{\text{decay}}^{\text{iso}}$  and indicates isolated direct photon production for  $R_\gamma^{\text{iso}} > 1$ . The subtraction procedure eliminates remaining background due to isolated decay photons that appear direct, which are due most often to asymmetric  $\pi^0 \rightarrow \gamma\gamma$  decays where the low  $p_T$  photon is not detected.

To suppress sources of background photons, tagging and isolation cuts are implemented at the event-by-event level. To reduce the contribution from decay photons, candidate inclusive photons are tagged and removed if a partner photon of  $p_T > 1$  GeV is found such that the invariant mass of the pair falls within the regions of 118–162 or 500–600 MeV/ $c^2$ . The tagging cuts use a larger  $\pi^0$  invariant mass range than for identifying  $\pi^0$  for dihadron correlations to err on the side of removing more decay photons. An isolation cut further suppresses decay photons as well as NLO fragmentation photons by requiring that the sum of the EMCAL energy deposits and  $p_T$  of charged tracks within a radius of 0.4 radians around the candidate photon be less than 10% of the photon’s total energy. To reduce the impact of detector acceptance effects, photons that pass the isolation and tagging cuts are also required to be  $\sim 0.1$  radians from the edge of the detector in both  $\eta$  and  $\phi$  forcing a large portion of the isolation cone to fall inside the PHENIX acceptance.

Because the number of isolated decay photons is not *a priori* known, the decay photon per-trigger yield is determined with a probability density function. Isolated  $\pi^0$ - $h^\pm$  correlated pairs are weighted by a probability density function to map these per-trigger yields to the isolated decay photon hadron correlated per-trigger yields. This function, determined in Ref. [50], gives the probability of an isolated  $\pi^0$  with  $p_T^{\pi^0}$  to decay to a photon with  $p_T^\gamma$  in the PHENIX acceptance where the photon was unable to be tagged as a decay photon. In the PHENIX central arms, the inability to tag a decay photon happens most often from asymmetric  $\pi^0$  decays, where one photon misses the detector completely. A 4% systematic uncertainty was assigned to the decay photon statistical subtraction method as a whole, which includes not considering backgrounds due to higher mass states such as the  $\eta$ ,  $\omega$ , and  $\rho$ . To determine the per-trigger yield of isolated decay pairs, the number of isolated  $\pi^0$ s is mapped via the probability function to the number of isolated decay pairs in a given  $p_T$  bin. The per-trigger yield of isolated decay pairs is then

$$Y_{\text{decay}}^{\text{iso}} = \frac{\sum_{N_\pi^{\text{iso}}} P(p_T^{\pi^0}, p_T^\gamma) N_{\pi-h}^{\text{iso}}}{\sum_{N_\pi^{\text{iso}}} P(p_T^{\pi^0}, p_T^\gamma) N_\pi^{\text{iso}}} \quad (6)$$

where  $P(p_T^{\pi^0}, p_T^\gamma)$  is the probability density function described above and contains all of the dependence and efficiencies of the detector on  $p_T^{\pi^0}$  and  $p_T^\gamma$ . The  $N_\pi^{\text{iso}}$  and  $N_{\pi-h}^{\text{iso}}$  are simply the number of isolated  $\pi^0$ -trigger par-

ticles measured and the number of isolated  $\pi^0$ - $h^\pm$  pairs measured, respectively.

The  $R_\gamma^{\text{iso}}$  is determined by measuring  $R_\gamma$  and correcting  $R_\gamma$  with tagging and isolation efficiencies. Because the quantity is the ratio of the inclusive photons to decay photons after tagging and isolation cuts, it can be written as

$$\begin{aligned} R_\gamma^{\text{iso}} &= \frac{N_{\text{inclusive}}^{\text{iso}}}{N_{\text{decay}}^{\text{iso}}} \\ &= \frac{N_{\text{inclusive}} - N_{\text{decay}}^{\text{tag}} - N_{\text{inclusive}}^{\text{niso}}}{N_{\text{decay}} - N_{\text{decay}}^{\text{tag}} - N_{\text{decay}}^{\text{niso}}} \\ &= \frac{R_\gamma}{(1 - \epsilon_{\text{decay}}^{\text{tag}})(1 - \epsilon_{\text{decay}}^{\text{niso}})} \frac{N_{\text{inclusive}} - N_{\text{decay}}^{\text{tag}} - N_{\text{inclusive}}^{\text{niso}}}{N_{\text{inclusive}}} \end{aligned} \quad (7)$$

where ‘‘niso’’ refers to ‘‘not isolated.’’ Because the tagging cuts are applied before the isolation cut,  $N_{\text{decay}}^{\text{tag}}$  is the number of photons tagged as decay photons regardless of the isolation cut, while  $N_{\text{inclusive}}^{\text{niso}}$  is the number of not isolated photons that were not able to be tagged.  $R_\gamma^{\text{iso}}$  is now written in terms of values that can be measured.  $R_\gamma$  and the tagging efficiency  $\epsilon_{\text{decay}}^{\text{tag}} = N_{\text{dec}}^{\text{tag}} R_\gamma / N_{\text{inclusive}}$  can be determined without the probability function because these quantities do not depend on possible isolated decay photons. The right-most fraction in Eq. 7 is simply the number of photons that pass the isolation and tagging cuts divided by the total number of inclusive photons and can be determined by counting the number of photons that pass the described cuts. The efficiency with which the isolation cut removes decay photons  $\epsilon_{\text{decay}}^{\text{niso}}$  is determined by applying the probability function at the level of the isolated parent meson and mapping the effect to the daughter photon

$$\epsilon_{\text{decay}}^{\text{niso}} = \left( 1 + \frac{\sum_\pi P(p_T^\pi, p_T^\gamma) \cdot N_\pi^{\text{iso}}}{\sum_\pi P(p_T^\pi, p_T^\gamma) \cdot N_\pi^{\text{niso}}} \right)^{-1} \quad (8)$$

Each of the quantities for determining  $R_\gamma^{\text{iso}}$  is found by counting the number of photons that pass the various cuts except for the isolation efficiency  $\epsilon_{\text{decay}}^{\text{niso}}$ , which is found by measuring the number of isolated and not isolated  $\pi^0$  that pass the cuts and weighting by the probability function as in Eq. 8.  $R_\gamma$  was found by dividing the number of inclusive photons  $N_{\text{inclusive}}$  by the number of decay photons  $N_{\text{decay}}$ ;  $N_{\text{decay}}$  was determined by counting the number of photons tagged from  $\pi^0$  decays and correcting for higher mass states and the PHENIX single and diphoton detection efficiencies derived from a GEANT-based simulation.  $\epsilon_{\text{decay}}^{\text{tag}}$  can then be calculated with  $R_\gamma$  and the number of tagged decay photons  $N_{\text{dec}}^{\text{tag}}$  and inclusive photons  $N_{\text{inclusive}}$ . As a cross check, systematic uncertainties on  $R_\gamma$  were evaluated using the direct photon and  $\pi^0$  pQCD cross sections with the CT10 PDFs [59] and DSS14 FFs [60]. The tagging efficiency is 0.36–0.43 and the isolation efficiency is 0.61–0.69 from

the lowest to highest  $p_T^{\text{trig}}$  bins. Note that each quantity in Eq. 7 is dependent only on  $p_T^{\text{trig}}$ . Figure 3 shows the values of  $R_\gamma^{\text{iso}}$  as a function of  $p_T^\gamma$ ; for which values greater than unity indicate isolated direct-photon production.

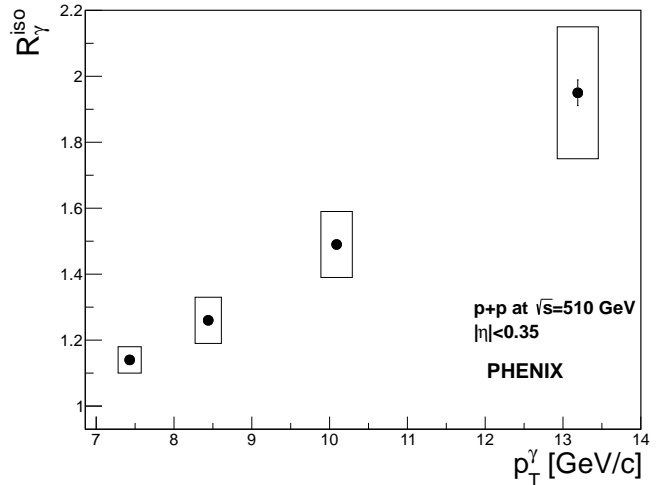


FIG. 3.  $R_\gamma^{\text{iso}}$  as a function of  $p_T^\gamma$ .

## IV. RESULTS

### A. Azimuthal Correlations

Figure 4 shows a few examples of the per-trigger yields of associated charged hadrons for both  $\pi^0$  and direct photon triggers as a function of  $\Delta\phi$  in bins of  $p_T^{\text{trig}}$  and  $p_T^{\text{assoc}}$ . The azimuthal correlations as a function of  $\Delta\phi$  show standard jet structure characteristics. The  $\pi^0$  yields show clear peaks at both  $\Delta\phi = 0$  and  $\Delta\phi = \pi$ , indicating nearly back-to-back jet production. The near-side yields of the isolated direct photons are not plotted, similarly to Ref. [61], because the yields within the isolation cone are physically uninterpretable. In addition, the effect of  $k_T$  smearing is characterized with the away-side peaks. The near-side  $\pi^0$  peaks are larger than the away sides due to the effect of so called ‘‘trigger bias,’’ discussed in Ref. [45]. The away-side yields of the direct photons are smaller than those from the  $\pi^0$  triggers due to the smaller jet energy sampled by direct photons; the  $\pi^0$  has some fractional energy  $z_{\pi^0} E_{\text{jet}}$  where  $z_{\pi^0}$  refers to the momentum fraction of the  $\pi^0$  from the scattered parton and  $E_{\text{jet}}$  is the energy of the jet, whereas the direct photon approximates the away-side jet energy at LO. The underlying event levels for  $\pi^0$  and direct photon triggers are similar, which would be expected if the underlying event structure is completely uncorrelated from the partonic hard scattering. A 9% normalization uncertainty on the charged hadron yields is not shown on this figure or any of the following per-trigger yields. This uncertainty is of similar magnitude to [50] and is largely due



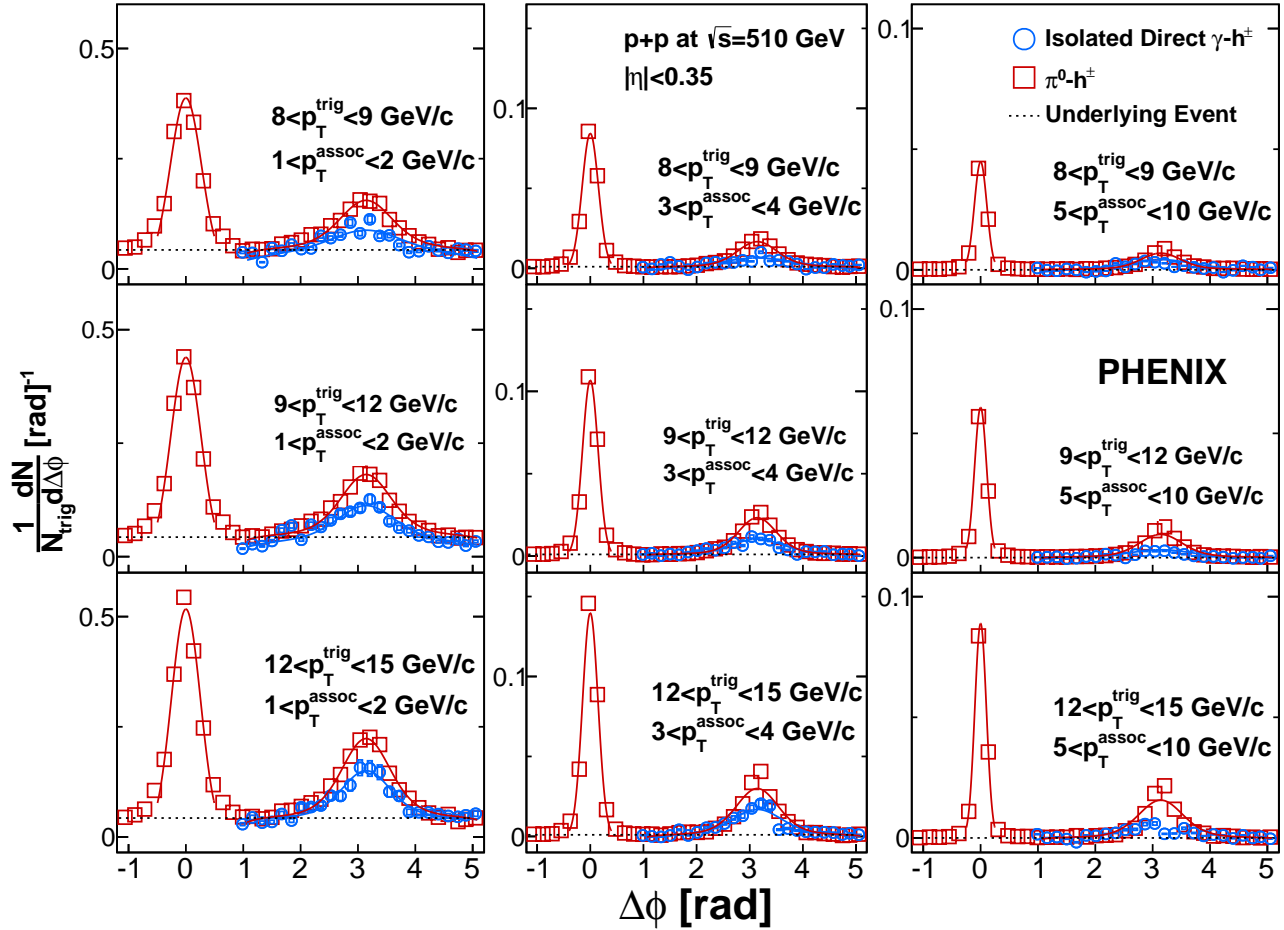


FIG. 5. Per-trigger yields as a function of  $\Delta\phi$  for the  $\pi^0$  correlation functions. The data points are shown for the  $\pi^0$  correlation functions (red squares) and the isolated direct  $\gamma$ - $h^\pm$  correlation functions (blue circles). The dotted line represents the underlying event. The plots are labeled with p+ p at  $\sqrt{s}=510$  GeV and  $|\eta|<0.35$ .

to the uncertainty when matching tracks from the DC to the PC. All of the per-trigger yields as a function of  $\Delta\phi$  can be found in the Supplemental Material [62].

### B. $\sqrt{\langle j_T^2 \rangle}$ Determination

The value  $\sqrt{\langle j_T^2 \rangle}$  was determined by the widths of Gaussian fits to the near-side of the  $\pi^0$  correlation functions, similarly to Ref. [45]. Examples of the fits are shown on the near-side  $\pi^0$  peaks in Fig. 4. Values of  $\sqrt{\langle j_T^2 \rangle}$  were calculated with the following equation

$$\sqrt{\langle j_T^2 \rangle} = \sqrt{2\langle j_T^2 \rangle} \simeq \sqrt{2} \frac{p_T^{\text{trig}} p_T^{\text{assoc}}}{\sqrt{p_T^{\text{trig}^2} + p_T^{\text{assoc}^2}}} \sigma_N \quad (9)$$

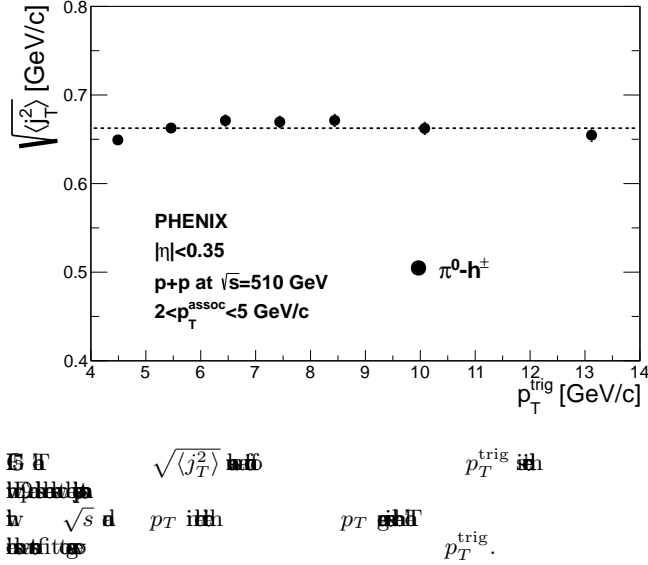
where  $\sigma_N$  is the Gaussian width. Previous measurements

have shown  $\sqrt{\langle j_T^2 \rangle}$  to be approximately constant with  $\sqrt{s}$  and  $p_T^{\text{trig}}$  in a similar  $p_T^{\text{trig}}$  range to that examined here [45, 46, 48, 63]. Only bins  $p_T^{\text{assoc}} > 2$  GeV/c were used to satisfy the assumption  $p_T^{\text{assoc}} \gg \sqrt{2} j_T$  which was made to determine Eq. 9. Each  $p_T^{\text{trig}}$  bin was fit to a constant and averaged  $\sqrt{\langle j_T^2 \rangle}$  over  $p_T^{\text{assoc}}$ . Figure 5 shows the results, which were then fit with a constant to average over  $p_T^{\text{trig}}$ , which is shown as a dotted line in Fig. 5. After averaging,  $\sqrt{\langle j_T^2 \rangle}$  was determined to be

$$\sqrt{\langle j_T^2 \rangle} = 0.662 \pm 0.003(\text{stat}) \pm 0.012(\text{sys}) \text{ GeV}/c \quad (10)$$

where the systematic uncertainty is due to the momentum resolution of the detector as well as approximations made to determine Eq. 9 in Ref. [45]. Recent ATLAS results show a similar fragmentation variable over a sig-

nificantly larger range of hundreds of GeV/c in  $p_T$ , and show that the average transverse momentum with respect to the jet axis rises slowly with  $p_T^{\text{jet}}$  over this significantly larger  $p_T$  range [64].



### C. $\sqrt{\langle p_{\text{out}}^2 \rangle}$ Determination

The quantity  $\sqrt{\langle p_{\text{out}}^2 \rangle}$  was extracted from the  $\Delta\phi$  correlations as was done in previous measurements<sup>1</sup> [45, 46, 50]. The value of  $\sqrt{\langle p_{\text{out}}^2 \rangle}$  quantifies the width of the away-side jet. The correlation functions are fit in bins of  $p_T^{\text{trig}}$  and  $p_T^{\text{assoc}}$  with the following function in the range  $\pi/3 < \Delta\phi < 5\pi/3$ :

$$\frac{dN}{d\Delta\phi} = C_0 + C_1 \cdot \frac{dN_{\text{far}}}{d\Delta\phi} \quad (11)$$

with

<sup>1</sup> We note that the fit function used here has the  $\sqrt{2}$  in the error function in the denominator, not the numerator as was done in the previous references. In order for the normalization of the function to be unity across the range  $[\pi/2, 3\pi/2]$  this  $\sqrt{2}$  should be in the denominator of the error function. We have studied the effect of this change and find that it does not change the value of  $\sqrt{\langle p_{\text{out}}^2 \rangle}$  extracted. This is because, as Fig. 31 of Ref. [45] shows, the quantity  $\sqrt{\langle p_{\text{out}}^2 \rangle}$  is determined from the exponential component of the fit function. The yield parameter extracted in Ref. [45] changes slightly, but within the quoted systematic uncertainties.

$$\frac{dN_{\text{far}}}{d\Delta\phi} = \begin{cases} 0 & |\Delta\phi - \pi| > \frac{\pi}{2} \\ \frac{-p_T^{\text{assoc}} \cos \Delta\phi}{\sqrt{2\pi \langle p_{\text{out}}^2 \rangle} \text{Erf}\left(\frac{p_T^{\text{assoc}}}{\sqrt{2\langle p_{\text{out}}^2 \rangle}}\right)} \times \exp\left(-\frac{|p_T^{\text{assoc}}|^2 \sin^2 \Delta\phi}{2\langle p_{\text{out}}^2 \rangle}\right) & |\Delta\phi - \pi| \leq \frac{\pi}{2}, \end{cases}$$

where the parameters  $C_0$ ,  $C_1$ , and  $\sqrt{\langle p_{\text{out}}^2 \rangle}$  are left as free parameters, with  $C_0$  quantifying the underlying event,  $C_1$  a normalization constant, and  $\sqrt{\langle p_{\text{out}}^2 \rangle}$  the parameter of interest. The fit extends to  $\pi/3$  and  $5\pi/3$  in order to accurately quantify the underlying event. Example fits are drawn on the correlation functions in Fig. 4. Systematic uncertainties were evaluated by altering the fit region by  $\pm 0.2$  radians and taking the absolute value of the difference of the resulting  $\sqrt{\langle p_{\text{out}}^2 \rangle}$ . The systematic uncertainties for the direct photons are larger due to the increased fluctuations in the underlying event due to the statistical subtraction technique.

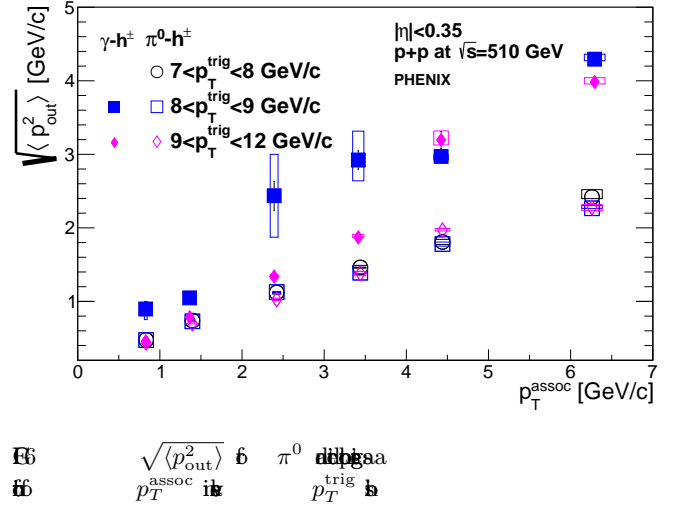
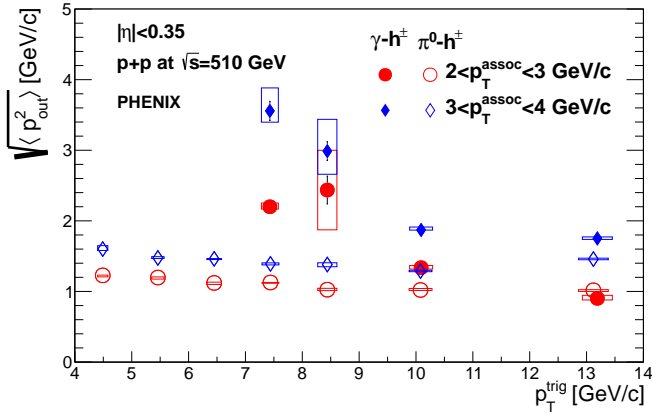


Figure 6 shows  $\sqrt{\langle p_{\text{out}}^2 \rangle}$  as a function of  $p_T^{\text{assoc}}$  in several  $p_T^{\text{trig}}$  bins for both  $\pi^0$  and direct photon triggers. All of the  $\sqrt{\langle p_{\text{out}}^2 \rangle}$  values can be found in Tables I and II of the Supplemental Material [62]. In the following figures showing measured quantities, filled points are for isolated direct photons and open points are for  $\pi^0$  triggers. Both  $\sqrt{\langle p_{\text{out}}^2 \rangle}$  distributions for  $\pi^0$  and direct photon triggers show a clear dependence on  $p_T^{\text{assoc}}$ , with the direct photons having a stronger dependence. The direct photon  $\sqrt{\langle p_{\text{out}}^2 \rangle}$  quantities are larger due to the smaller jet energy being sampled compared to the  $\pi^0$  jet energies. The strong dependence of  $\sqrt{\langle p_{\text{out}}^2 \rangle}$  on  $p_T^{\text{assoc}}$  is anticipated as could be ascertained from the definition of  $p_{\text{out}} = p_T^{\text{assoc}} \sin \Delta\phi$ . In the same  $\Delta\phi$  region, as  $p_T^{\text{assoc}}$  gets larger,  $p_{\text{out}}$  will also get larger.

Figure 7 shows a subset of the  $\sqrt{\langle p_{\text{out}}^2 \rangle}$  results for both direct photon and  $\pi^0$  triggers as a function of  $p_T^{\text{trig}}$  in the  $p_T^{\text{assoc}}$  range 2–4 GeV/c. The  $\pi^0$ -triggered  $\sqrt{\langle p_{\text{out}}^2 \rangle}$

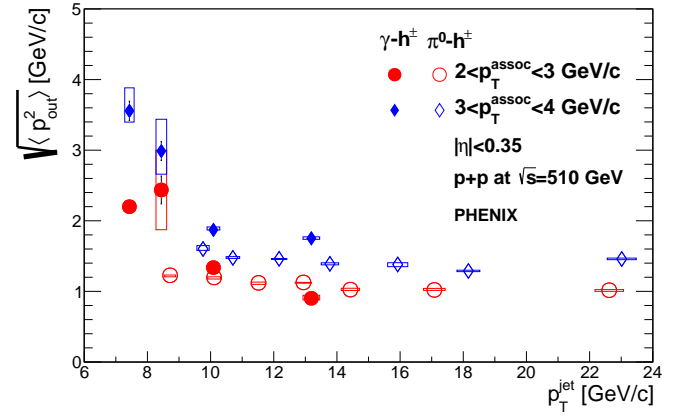
decreases with  $p_T^{\text{trig}}$ , although this dependence is small. The direct photons clearly have a strong dependence on  $p_T^{\text{trig}}$  relative to the  $\pi^0$  triggers. The  $\pi^0$  data shown in Fig. 7 contain a dependence on the fragmentation function not present in the direct photon data because the direct photons emerge directly from the hard scattering. To explore this dependence, PYTHIA 6.4 [65] hard-scattered QCD events were analyzed to determine the average  $z_T = p_T^{\text{trig}}/\hat{p}_T^{\text{trig}}$  of a  $\pi^0$  where the hat quantity refers to the hard scattered parton.  $\langle z_T^{\pi^0} \rangle$  was determined in the same bins used in the data to correct the  $\pi^0$   $p_T^{\text{trig}}$  to an estimated jet  $p_T$  in order to make a better comparison between the direct photons and  $\pi^0$ . Figure 8 shows the same  $\sqrt{\langle p_{\text{out}}^2 \rangle}$  plotted as a function of  $p_T^{\text{jet}}$ , where  $p_T^{\text{jet}}$  refers to  $p_T^{\text{trig}}$  for the direct photons and to  $p_T^{\text{trig}}/\langle z_T^{\pi^0} \rangle$  for the  $\pi^0$ . The  $\langle z_T^{\pi^0} \rangle$  correction ranges from 0.45–0.63 as a function of  $p_T^{\text{trig}}$ . After the correction, the  $\pi^0$  and direct photon  $\sqrt{\langle p_{\text{out}}^2 \rangle}$  do not appear to form a single continuous function; rather the  $\pi^0$   $\sqrt{\langle p_{\text{out}}^2 \rangle}$  continue approximately linearly to lower  $p_T^{\text{jet}}$ . It is possible that the the stronger dependence of  $\sqrt{\langle p_{\text{out}}^2 \rangle}$  on  $p_T^{\text{trig}}$  for the direct photons is due to the smaller jet energy being probed. This effect may also be seen for the low  $p_T^{\text{trig}}$  dihadron correlations in Table II of Ref. [46], where  $\sqrt{\langle p_{\text{out}}^2 \rangle}$  has been observed to show a stronger dependence at small  $p_T^{\text{trig}}$  than for larger  $p_T^{\text{trig}}$ .



**E7**  $\sqrt{\langle p_{\text{out}}^2 \rangle}$   $\pi^0$   $\gamma$   $\pi^0$   $\gamma$   
**E8**  $p_T^{\text{trig}}$   $p_T^{\text{trig}}$   $p_T^{\text{assoc}}$   $p_T^{\text{assoc}}$   $\pi^0$   $\gamma$   $\pi^0$   $\gamma$   
 PYTHIA.

#### D. $p_{\text{out}}$ Distributions

Figure 9 shows the per-trigger yields of the  $p_{\text{out}}$  distributions for  $\pi^0$  and direct photon triggers. Only away-side hadrons were used in making the distributions, with the requirement that the correlated hadron satisfy  $2\pi/3 < \Delta\phi < 4\pi/3$ . The underlying event was statistically subtracted out from the  $p_{\text{out}}$  per-trigger yields using the parameters from the fits to the  $\Delta\phi$  correlations with Eq. 11



**E8**  $\sqrt{\langle p_{\text{out}}^2 \rangle}$   $\pi^0$   $\gamma$   $\pi^0$   $\gamma$   
**E9**  $p_T^{\text{jet}}$   $p_T^{\text{jet}}$   $p_T^{\text{assoc}}$   $p_T^{\text{assoc}}$   $\pi^0$   $\gamma$   $\pi^0$   $\gamma$   
 PYTHIA.

in order to identify only charged hadron yield associated with the hard scattering. The underlying event yield for a given bin was statistically subtracted by applying a factor  $N_{\text{UE}} = 1 - f(\Delta\phi)$  where  $f(\Delta\phi)$  is the correction function determined by  $C_0$  divided by the fits to the  $\Delta\phi$  correlations. For the smaller  $p_T^{\text{trig}}$  bins, this is an important subtraction because in the signal region  $\Delta\phi \sim \pi$  the underlying event contributes roughly 50% of the away-side yield, as could be ascertained from Fig 4. The yield corrected by the underlying event factor  $N_{\text{UE}}$  is then subjected to the usual construction of the correlation function outlined in Sec. III. Systematic uncertainties on the underlying event background subtraction were evaluated by performing the subtraction after changing the underlying event parameter  $C_0$  to  $C_0 \pm 1\sigma$ , where  $\sigma$  is the error on  $C_0$  from the fit. These uncertainties were found to be on the order of tenths of a percent in the  $p_{\text{out}} \approx 0$  region. The values of the  $p_{\text{out}}$  distributions can be found in Tables III-XIII of the Supplemental Material [62]. Note that a 4% systematic uncertainty is assigned to  $p_{\text{out}}$  due to the detector resolution on  $p_T^{\text{assoc}}$  and  $\Delta\phi$ .

The distributions are fit with a Gaussian at small  $p_{\text{out}}$  in the region  $[-1.1, 1.1]$  GeV/c as well as a Kaplan function over the whole range, with the Kaplan function parameterized by  $a(1 + \frac{p_{\text{out}}^2}{b})^{-c}$  where  $a$ ,  $b$ , and  $c$  are free parameters. In Fig. 9 the solid lines are fits to the  $\pi^0$  distributions and the dashed lines are fits to the isolated direct photon distributions. The Gaussian functions clearly fail past  $\sim 1.3$  GeV, showing a transition to power law behavior which the Kaplan functions accurately describe. The power law behavior is generated from hard gluon radiation in the initial state or final state, whereas the Gaussian behavior is generated from the soft  $k_T$  and  $j_T$  and is demonstrated in the nearly back-to-back hadrons that are produced around  $p_{\text{out}} \approx 0$ .

The evolution of  $p_{\text{out}}$  as a function of  $p_T^{\text{trig}}$  was characterized by the Gaussian widths at small  $p_{\text{out}}$ . Figure 10 shows the widths from Gaussian fits to both  $\pi^0$  and di-

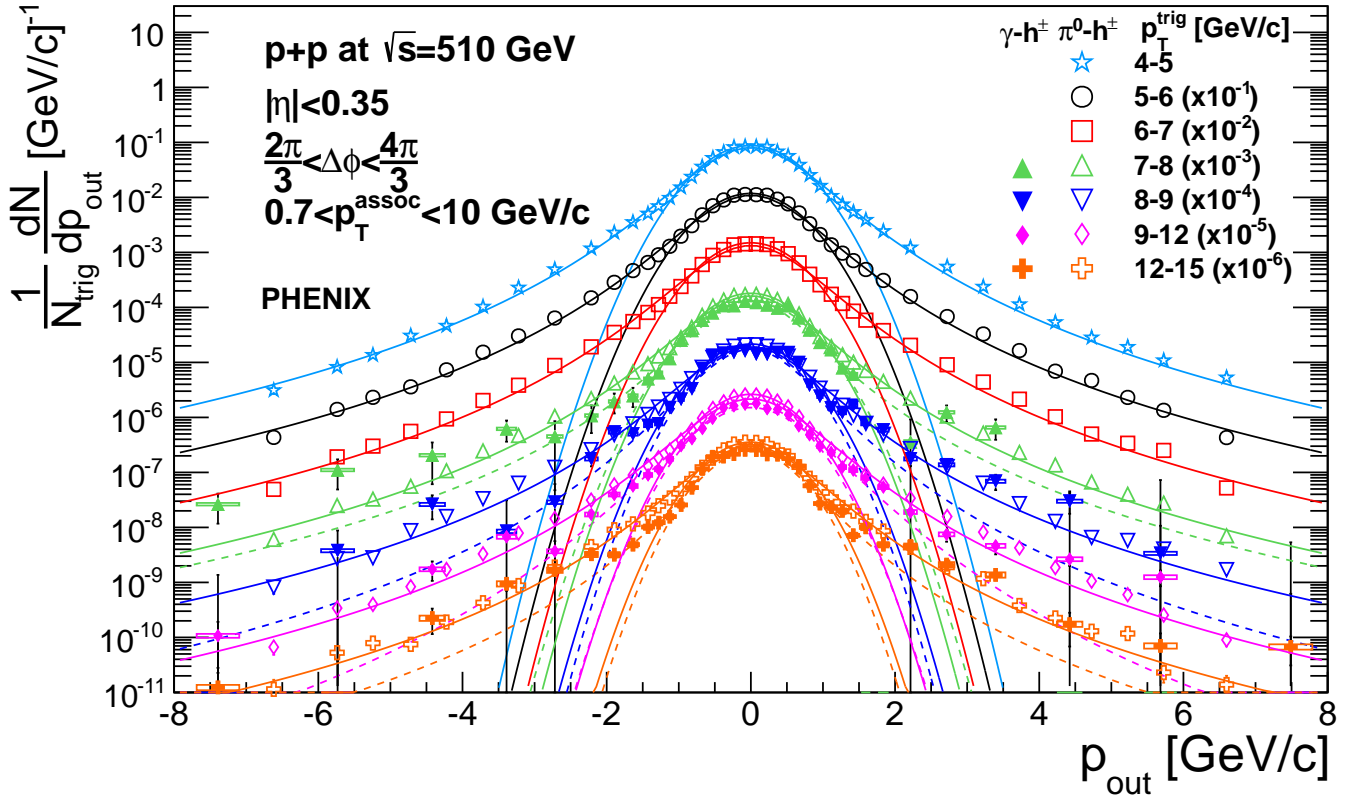


FIG. 10. PHENIX  
 660n  
 10a  
 10b  
 10c  
 10d  
 10e  
 10f  
 10g  
 10h  
 10i  
 10j  
 10k  
 10l  
 10m  
 10n  
 10o  
 10p  
 10q  
 10r  
 10s  
 10t  
 10u  
 10v  
 10w  
 10x  
 10y  
 10z

$p_{out}$   $k_T$

$p_{out}$   $\pi^0$

rect photon triggers as a function of  $p_T^{\text{trig}}$ . Systematic uncertainties were evaluated by altering the Gaussian fit region by  $\pm 0.15$  GeV/c and taking the absolute value of the difference of the resulting widths. As the systematic uncertainties dominate the uncertainties of the widths, the error bars shown in Fig. 10 are the statistical and systematic uncertainties combined in quadrature. Similarly to  $\sqrt{\langle p_{out}^2 \rangle}$ , the direct photons and  $\pi^0$  both show decreasing widths with  $p_T^{\text{trig}}$ . Linear fits to the two sets of widths give slopes of  $-0.0055 \pm 0.0018(\text{stat}) \pm 0.0010(\text{syst})$  for  $\pi^0$  mesons and  $-0.0109 \pm 0.0039(\text{stat}) \pm 0.0016(\text{syst})$  for direct photons. Systematic uncertainties on the slopes were conservatively estimated by evaluating the fit when the points were placed at the limits given by the systematic uncertainties, and then taking the difference of the slopes. Similarly to  $\sqrt{\langle p_{out}^2 \rangle}$  the  $\pi^0$  triggers were corrected by the same  $\langle z_T^{\pi^0} \rangle$  corrections from PYTHIA. The result is shown in Fig. 11; again the  $\langle z_T^{\pi^0} \rangle$  correction amounts to a scale factor of approximately two for the  $p_T^{\text{trig}}$  of the  $\pi^0$  triggers. When plotted against  $p_T^{\text{trig}}/\langle z_T^{\pi^0} \rangle$  the magnitude of the slope for the  $\pi^0$  triggers is  $-0.0035 \pm 0.0012(\text{stat}) \pm 0.0006(\text{syst})$ . It should be noted that the slope of the widths changes if the minimum  $p_T^{\text{assoc}}$  cut is increased, but that the slope al-

ways remains negative. Integrating over the full range of  $0.7 < p_T^{\text{assoc}} < 10$  GeV/c allowed by the PHENIX detector gives the smallest magnitude slope, thus it is the most conservative measurement for comparing to CSS evolution. For example, the slope of the Gaussian widths of  $p_{out}$  for  $1.2 < p_T^{\text{assoc}} < 10$  GeV/c was determined to be  $-0.012 \pm 0.003(\text{stat}) \pm 0.001(\text{syst})$  for  $\pi^0$ -meson and  $-0.023 \pm 0.007(\text{stat}) \pm 0.003(\text{syst})$  for direct-photon triggers. The same behavior can be seen in the values of  $\sqrt{\langle p_{out}^2 \rangle}$  in Fig. 7 and in the Supplemental Material [62].

## V. DISCUSSION

### A. Measured Results

Figures 7 and 10 show that, consistent with previous RHIC measurements,  $\sqrt{\langle p_{out}^2 \rangle}$  and the Gaussian widths of  $p_{out}$  sensitive to initial-state and final-state  $k_T$  and  $j_T$  decrease with the hard scale. Interpretation of  $\sqrt{\langle p_{out}^2 \rangle}$  is slightly different than that of the Gaussian widths from the  $p_{out}$  distributions, because the Gaussian widths are extracted from fits to the nearly back-to-back region, which is generated only by nonperturbative  $k_T$  and  $j_T$ . The  $\sqrt{\langle p_{out}^2 \rangle}$  values are extracted from fits to

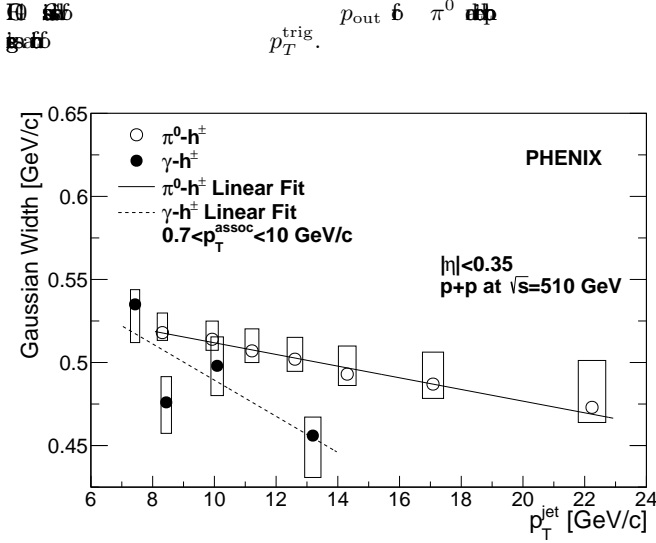
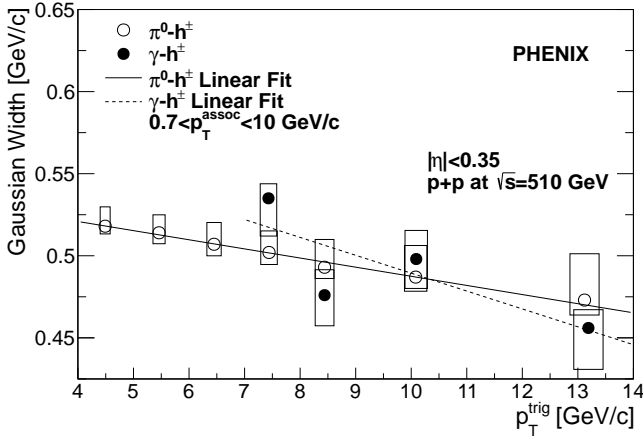


FIG. 10. (a) Inclusive- $\pi^0$  and (b) direct-photon production. The Gaussian widths are shown as a function of the trigger transverse momentum  $p_T^{\text{trig}}$  (left) and the away-side jet transverse momentum  $p_T^{\text{jet}}$  (right). The data points are shown for  $\pi^0$  (open circles) and  $\gamma$  (filled circles) triggers. The solid lines represent the linear fits to the data, and the dashed line represents the linear fit to the  $\gamma$ - $h^{\pm}$  data. The plot is for  $|\eta| < 0.35$ ,  $p+p$  at  $\sqrt{s} = 510$  GeV, and  $0.7 < p_T^{\text{assoc}} < 10$  GeV/c.

the entire away-side jet region in the  $\Delta\phi$  correlations; therefore, these quantities inherently include the charged hadrons in the perturbatively generated tail away from  $\Delta\phi \sim \pi$  whereas the Gaussian widths measured from the  $p_{\text{out}}$  distributions *only* have contributions from  $\Delta\phi \sim \pi$ . Nonetheless the values of  $\sqrt{\langle p_{\text{out}}^2 \rangle}$  are dominated by the nearly back-to-back region as this is where most of the away-side charged hadrons are, but this subtle difference between the two observables should be noted. The widths quantified by  $\sqrt{\langle p_{\text{out}}^2 \rangle}$  have the benefit that they can be extracted from the finely binned  $p_T^{\text{trig}} \otimes p_T^{\text{assoc}}$   $\Delta\phi$  angular correlations. Throughout this discussion, we will use the term “width” to refer to both the  $\sqrt{\langle p_{\text{out}}^2 \rangle}$  and Gaussian widths extracted from  $p_{\text{out}}$ .

There is a difference in the mix of scattered away-side partons probed by inclusive- $\pi^0$  and direct-photon triggers. Figure 12 shows the fractional contribution to the total cross section calculated in pQCD for the LO di-

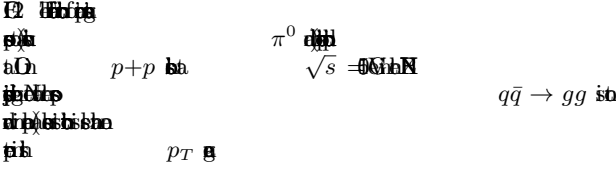
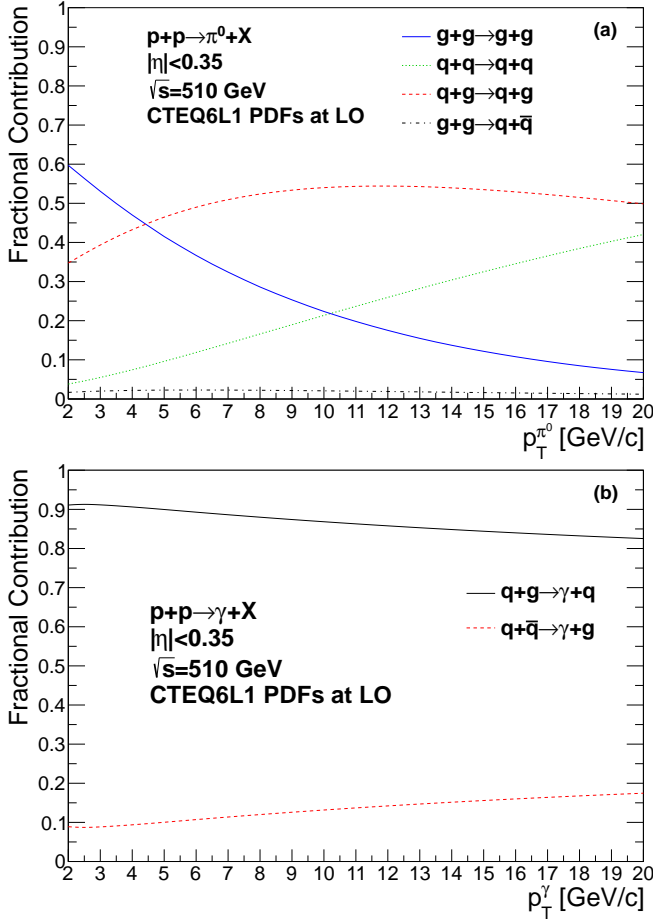
Trigger Type	$\langle p_T^{\text{trig}} \rangle$ [GeV/c]	Gaussian Width [GeV/c]
$\pi^0$	4.49	$0.518^{+0.012}_{-0.005}$
	5.46	$0.514^{+0.011}_{-0.007}$
	6.45	$0.507^{+0.013}_{-0.007}$
	7.44	$0.502^{+0.013}_{-0.007}$
	8.44	$0.493^{+0.017}_{-0.007}$
	10.1	$0.487^{+0.019}_{-0.009}$
	13.1	$0.473^{+0.028}_{-0.009}$
Direct photon	7.43	$0.535^{+0.009}_{-0.023}$
	8.44	$0.476^{+0.015}_{-0.019}$
	10.1	$0.498^{+0.017}_{-0.018}$
	13.2	$0.456^{+0.011}_{-0.025}$

agrams for (a) inclusive- $\pi^0$  and (b) direct-photon production. The CTEQ6L1 [66] PDFs were used for the calculations in addition to the DSS14 FFs [60] for the  $\pi^0$ . At LO, quark-gluon Compton scattering accounts for approximately 85% of direct photons produced at midrapidity, while  $\pi^0$  triggers are instead generated by a significant contribution of  $qg$ ,  $gg$ , and  $qq$  scatterings. Therefore, any comparison between direct photon and  $\pi^0$  triggers could be affected by the fact that the away-side charged hadrons are produced by quark jets  $\sim 85\%$  of the time for direct photons and a mix of gluon and quark jets for the  $\pi^0$ . For the direct photon partonic fractions, NLO corrections do not make a significant difference in the dominance of the quark-gluon Compton scattering process in the central rapidity region studied here [67].

Many correlation measurements similar to the one presented here have been made at RHIC [45, 46, 50, 68], as discussed in the Introduction. Although the same conclusion regarding the evolution of the widths found here can be drawn from these measurements, they were made with different physics goals; examples include understanding partonic energy loss in a nuclear medium or characterizing fragmentation functions. Earlier correlation measurements were largely motivated by the heavy ion or hard scattering high-energy-physics community, and it was not until recently that the nucleon-structure community began to understand how to look for possible factorization breaking effects in these types of measurements [69]. This came as a result of the recent interest in understanding TMD evolution, especially understanding the nonperturbative contributions to TMD evolution. Reference [39] gives a comprehensive discussion of phenomenology including TMD evolution and how this phenomenology came to the forefront in 2011.

## B. Expectations from CSS Evolution

Consistent with previous measurements, the data presented here clearly show that momentum widths sensitive to nonperturbative  $k_T$  and  $j_T$  decrease with the hard



scale in  $\pi^0$ - and direct photon-charged hadron correlations. As was mentioned in the Introduction, the expectation from CSS evolution is that momentum widths sensitive to nonperturbative transverse momentum scales should increase with the hard scale. To compare to what is predicted by CSS evolution, the slopes were compared to a slope of zero as this quantifies the boundary between narrowing and increasing widths with  $p_T^{\text{trig}}$ . The confidence interval excludes a slope of zero at the  $2.6\sigma$  level for both the  $\pi^0$  and direct photon triggered correlations. The likelihood ratio from a slope of zero was calculated to be 0.03 for both the  $\pi^0$  and direct photon triggered correlations, which implies that the data is not consistent with a flat line.

Because  $k_T$  and  $j_T$  have been measured to be approximately constant in the  $p_T^{\text{trig}}$  region probed here [45, 50], kinematically it would be expected that the acoplanarity decrease with  $p_T^{\text{trig}}$ . However, this same argument would apply for both DY and SIDIS, showing that the effect

of decreasing widths seen in  $\pi^0 - h^\pm$  and direct  $\gamma - h^\pm$  correlations cannot be a kinematic or fragmentation effect alone. It is also interesting that Ref. [51] shows that in dijet correlations at very high  $p_T$  and  $\sqrt{s}$ , momentum widths sensitive to initial-state  $k_T$  increase with the  $p_T$  of the jet. These measurements are at large  $p_T$  and sensitive to large  $k_T$  at the higher  $\sqrt{s}$  of the Large Hadron Collider, and thus follow the leading-log approximation which is also purely perturbative and predicts increasing widths with the hard scale (see e.g. [70] and references within).

The CSS evolution framework was motivated by understanding perturbative QCD dynamics. At this time, QCD was still in the early stages of development, and nonperturbative dynamics were not the focus within the framework of pQCD. As QCD became well established as the theory of the strong force, measurements performed at high enough energies for perturbative techniques to be applicable began to be used routinely to constrain nonperturbative physics in the form of collinear PDFs and FFs. It is only in the last two decades that there has been increasing focus on using perturbative techniques to understand nonperturbative parton dynamics. The study of such nonperturbative dynamics provides information on parton behavior within bound states and the process of hadronization by defining and constraining TMD PDFs and FFs. Importantly, it is additionally offering new insights on fundamental aspects of QCD as a nonAbelian gauge-invariant quantum field theory, for example through the predicted relative sign difference of the Sivers TMD PDF when probed via SIDIS versus DY [27], and through TMD factorization breaking in certain processes [28]. Factorization breaking results from basic QCD principles. Namely, nonAbelian phase interferences from the exchange of gluons between colored objects cannot, in general, be disentangled. Similarly, phase interferences from gluon exchange play a role in the Sivers effect where it implies a sign change for the Sivers function between DY and SIDIS interactions. The reason that gluon exchange in DY and SIDIS does not lead to factorization breaking is because DY and SIDIS are both quantum electrodynamic processes at LO, so there are limited paths for gluon exchange. Only initial-state exchange in DY and final-state exchange in SIDIS are possible, whereas in hadronic collisions with a final-state hadron measured both initial- and final-state exchanges are possible.

Observing differences in the evolution of momentum widths as a function of the hard scale is a powerful observable due to the qualitative conclusion that can be drawn from the data when comparing to the expectation of CSS evolution. Before the recent interest in understanding TMD evolution, measured deviations from calculations at some given scale assuming factorization holds were the only obvious way to look for factorization breaking effects. Such calculations are not available. Simply looking for qualitative differences in the evolution of the observable gives a clear discrepancy with the

expectation from CSS evolution, and this is significantly more powerful than trying to compare with a calculation that requires greater knowledge of the nonperturbative functions. It is furthermore interesting to point out that the inclusive hadron transverse single-spin asymmetries in hadronic collisions measured at forward rapidities also deviate from the expectation provided by standard perturbative evolution. In charged pion production, the asymmetry changes strikingly little from  $\sqrt{s} = 4.9$  GeV to  $\sqrt{s} = 62.4$  GeV [71]. Asymmetries have been measured to be nonzero at center of mass energies up to 200 GeV and appear to plateau at  $p_T$  up to 5 GeV/c [72], while perturbative techniques give a clear prediction that the asymmetry should fall off as  $p_T$  increases [73].

### C. Comparison to PYTHIA

Without any available theoretical calculations of our observable, the results found in the data as well as the expectation from CSS evolution were investigated with a PYTHIA simulation. Factorization breaking is not predicted in DY production because there are no final-state hadrons produced directly from the hard scattering. The same observable  $p_{\text{out}}$  can be constructed in DY events with two nearly back-to-back leptons. For dileptons, it would be expected that the Gaussian width of  $p_{\text{out}}$  would broaden as one increases the hard scale of the interaction, as DY is known to follow CSS evolution. The Perugia0 tune [74] should be ideal to study this because it was tuned to the CDF  $Z^0$  cross section data at low  $p_T$  [75]. Therefore the Perugia tunes should be reasonably adequate at reproducing DY events where the total  $p_T$  is small.

PYTHIA 6.4 DY events were generated and  $p_{\text{out}}$  was determined for the correlated dileptons to confirm the expectation from CSS evolution for this observable.  $p_{\text{out}}$  is defined similarly to Eq. 1,  $p_{\text{out}} = p_T^{\text{lep}} \sin \Delta\phi$  where the higher- $p_T$  lepton is taken as the near-side trigger particle and the lower- $p_T$  lepton is taken as the away-side associated particle used in the determination of  $p_{\text{out}}$ . The distributions were fit with Gaussian functions in the non-perturbative nearly back-to-back region, and the widths of the dilepton  $p_{\text{out}}$  distributions are shown in Fig. 13. PYTHIA reproduces the expectation that the widths of the DY pairs increase with the  $Q^2$  of the interaction when  $p_{\text{out}}$  is only sensitive to initial-state  $k_T$  and there are no final-state hadrons. The widths are quantitatively much larger than the dihadron or direct photon-hadron widths because the DY dileptons emerge from the virtual photon, which means that, in the PHENIX pseudorapidity region, their  $p_T$  is large. When measuring a final-state hadron,  $p_{\text{out}}$  by definition must be smaller for the case of a measured final-state hadron vs. a DY lepton because the  $p_T$  of the charged hadron must be smaller than or equal to the  $p_T$  of the scattered parton due to the fragmentation process. Any quantitative value of  $p_{\text{out}}$  will naturally be dependent on the  $p_T^{\text{assoc}}$  measured; see Fig. 6.

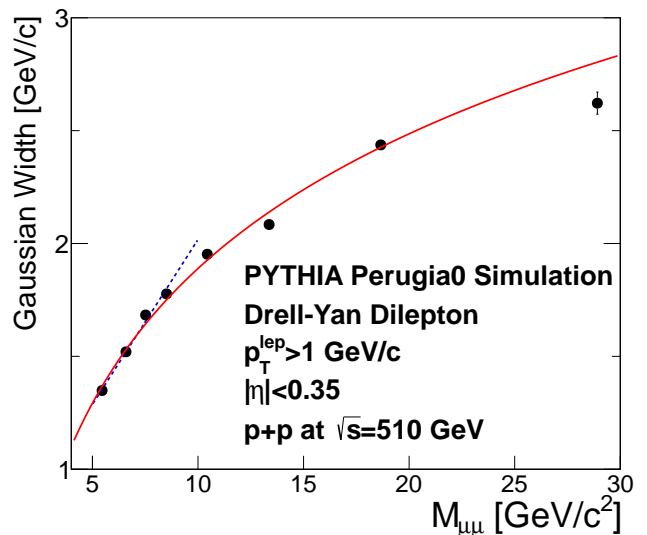


FIG. 13. Gaussian widths of the correlated dilepton  $p_{\text{out}}$  distributions for the PYTHIA Perugia0 simulation. The blue dotted line shows a linear fit to the data in the region  $5 < M_{\mu\mu} < 10 \text{ GeV}/c^2$ , and the red solid line shows a log fit to the data over the full invariant mass range. The simulation parameters are  $p_T^{\text{lep}} > 1 \text{ GeV}/c$  and  $|\eta| < 0.35$ , p+p at  $\sqrt{s} = 510 \text{ GeV}$ .

In DY, each lepton will have approximately half the momentum of the interaction hard scale, and the larger the momentum of the larger  $p_{\text{out}}$  can be while still being in the nearly back-to-back region  $\Delta\phi \sim \pi$ , i.e. nonperturbatively generated. What is relevant is the evolution of this width with the hard scale of the interaction, not the quantitative value, as this is just indicative of what away-side  $p_T^{\text{assoc}}$  is observed. The DY widths were fit with a linear function shown as the blue dotted line in the region which was most linear, 5–10 GeV/c<sup>2</sup>, and the slope of the line was determined to be  $0.146 \pm 0.004$ . Additionally the red solid line shows a log fit over the full invariant mass range. The DY slope is the opposite sign from the direct photon-hadron and dihadron correlations and it is also approximately one order of magnitude larger making it significantly different from the dihadron and direct photon-hadron slopes.

Similarly, PYTHIA direct photon and dijet events were generated at  $\sqrt{s} = 510$  GeV with the Perugia0 tune, changing the Gaussian intrinsic  $k_T$  parameter PARP(91) setting to 3.2 GeV/c as should be expected at  $\sqrt{s} = 510$  GeV from Ref. [45]. The Perugia0 tune was used again for the dihadron and direct photon-hadron correlations so that a direct comparison could be made to the DY Perugia0 tune Gaussian widths. The direct photons were required to be isolated similarly to what was done in data. Correlated pairs of  $\pi^0$  or direct photon and  $\pi^\pm$ ,  $K^\pm$ , and  $p, \bar{p}$  were collected in the PHENIX pseudorapidity, and the observables  $\Delta\phi$  and  $p_{\text{out}}$  were determined from the correlated pairs. Similarly to what was done in data, the background from the underlying event was statistically

subtracted out to make the  $p_{\text{out}}$  distributions. PYTHIA correlated pairs show the same features as the data do as can be seen in Fig. 14;  $p_{\text{out}}$  exhibits a Gaussian shape at small  $p_{\text{out}}$  which transitions to a power law shape at large  $p_{\text{out}}$ .

Gaussian widths were extracted from the PYTHIA-generated correlations in the same way that was done for the data. The widths from the PYTHIA  $p_{\text{out}}$  distributions are shown with the measured widths in Fig. 15. Remarkably, the PYTHIA results reproduce the measured slopes in both sign and magnitude for both  $\pi^0$  and direct photon triggers. The slope values from PYTHIA were  $-0.0056 \pm 0.0007$  for  $\pi^0$ -meson  $-0.0107 \pm 0.0006$  for direct-photon triggers. The measured slopes are  $-0.0055 \pm 0.0018(\text{stat}) \pm 0.0010(\text{syst})$  for  $\pi^0$ -meson and  $-0.0109 \pm 0.0039(\text{stat}) \pm 0.0016(\text{syst})$  for direct-photon triggers. The negative sign of the slope was found in both the quark-gluon Compton and quark-antiquark annihilation processes for isolated direct photon production, indicating that the effect in PYTHIA is not due to a difference in quark vs. gluon fragmentation. Additionally, as the minimum  $p_T^{\text{assoc}}$  cut is increased when constructing the  $p_{\text{out}}$  distributions, the slope of the Gaussian widths increases, similarly to what is seen in data. One noticeable difference between PYTHIA and the data is the quantitative values of the widths. Here the results from PYTHIA differ by about  $\sim 15\%$  for both the  $\pi^0$  and direct photon triggers, depending on the  $p_T^{\text{trig}}$  bin.

The nonperturbative Gaussian behavior of  $p_{\text{out}}$  is generated by the soft initial-state  $k_T$  and final-state  $j_T$  as indicated in Fig. 1. In the nearly back-to-back region  $p_{\text{out}} \lesssim 1.3 \text{ GeV}/c$ ,  $p_{\text{out}}$  is small and thus can only be generated by soft gluon radiation because the two particles are nearly coplanar. It is unsurprising that PYTHIA does not replicate the quantitative values of the Gaussian widths well as there is little data that would offer constraints to this region. What is striking is that PYTHIA replicates the evolution rate for both  $\pi^0$  and direct photon Gaussian widths.

While PYTHIA certainly does not explicitly consider analytical factorization breaking effects as it assumes collinear factorization, in contrast to a collinear pQCD calculation it does include initial- and final-state interactions. After a parton interacts in PYTHIA, the remnants of the two protons are free to interact with other objects in the event, and every object in the interaction is forced to color neutralize. Factorization breaking effects are predicted in dihadron and direct photon-hadron correlations due to the possibility of gluon exchange in both the initial and final states. This includes gluon exchange with remnants of the interaction, because the remnants of the interacting protons can exchange gluons with partons in both the initial and final states. Sensitivity to these effects requires a small transverse momentum scale; in the transverse-momentum-integrated case observables no longer have this sensitivity. For this reason it is plausible that PYTHIA could be sensitive to these effects because of interactions between the proton remnants and

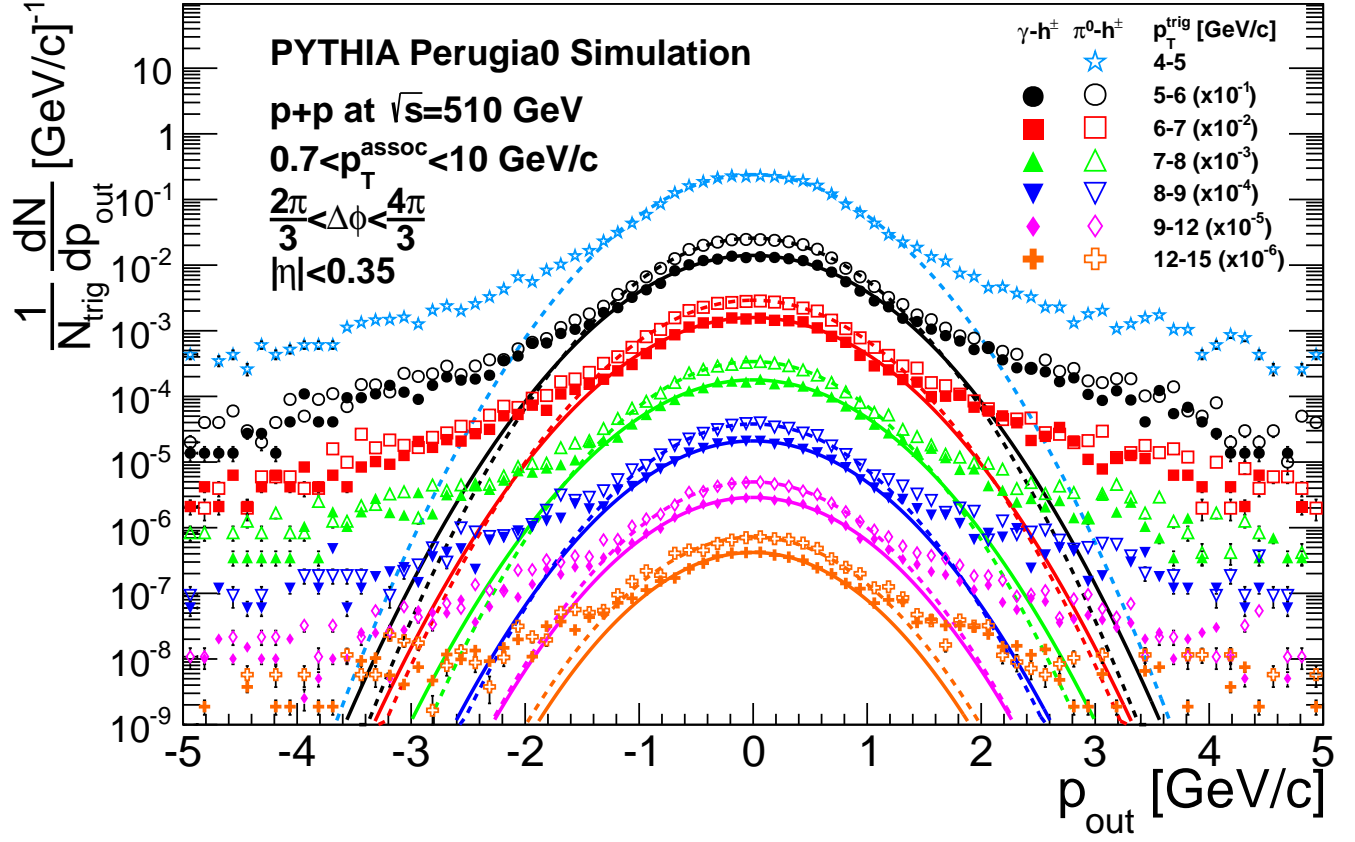
partons involved in the hard scattering. Because PYTHIA allows initial- and final-state interactions via gluon exchanges, the necessary interactions to allow for factorization breaking effects are present within the PYTHIA framework. It should also be noted that PYTHIA replicates the color coherence effects in Refs. [32–34] as well.

The underlying mechanism that leads to the prediction of the sign change in the Siverson function or factorization breaking is gluon exchange between partons associated with the hard scattering and colored remnants. In cases where factorization breaking is predicted, it implies that the traditional organization of the nonperturbative objects into separate PDFs and FFs for each colliding proton and produced hadron no longer holds. However, so far we have no knowledge of how to approach a reorganization of the nonperturbative objects, which would presumably include novel correlation functions describing partons correlated across the colliding protons. The fact that PYTHIA accurately describes both the qualitative and quantitative nature of the slopes of the widths as a function of hard scale offers a potential path forward to greater understanding and further advancing what can be calculated within the rigors of pQCD.

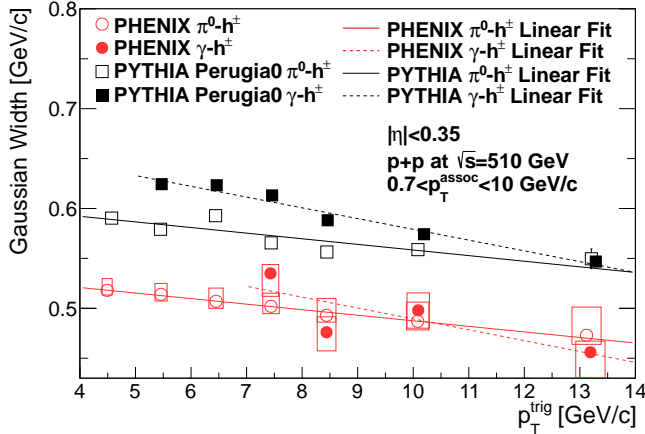
## VI. SUMMARY AND CONCLUSIONS

Dihadron and direct photon-hadron correlations sensitive to nonperturbative transverse momentum effects have been measured in the PHENIX experiment at RHIC in  $\sqrt{s} = 510 \text{ GeV}$   $p+p$  collisions, motivated by the prediction of factorization breaking in such processes [28–31]. Correlations between  $\pi^0$  or direct photons with charged hadrons were measured. The azimuthal angular separation  $\Delta\phi$  and out-of-plane transverse momentum component  $p_{\text{out}}$  for the correlated pairs were measured.  $p_{\text{out}}$  has sensitivity to nonperturbative transverse momentum in the initial state, as well as in the final state when a produced hadron is measured. The  $\sqrt{\langle p_{\text{out}}^2 \rangle}$  and Gaussian widths of the  $p_{\text{out}}$  distributions were measured from the correlations, and both observables decrease with the hard scale of the interaction  $p_T^{\text{trig}}$ . The direct photons exhibit a larger dependence than the  $\pi^0$  triggers on  $p_T^{\text{trig}}$  for both  $\sqrt{\langle p_{\text{out}}^2 \rangle}$  and the Gaussian widths of  $p_{\text{out}}$ . The narrowing of the Gaussian widths as a function of  $p_T^{\text{trig}}$  indicates that the Collins-Soper-Sterman soft factor cannot be driving the evolution, in contrast with Drell-Yan dilepton production and SIDIS where factorization is predicted to hold and the widths are empirically known to increase with hard scale. Study of the same observables via the PYTHIA event generator, which allows for gluon exchange between partons involved in the hard scattering and the proton remnants, reveals strikingly similar characteristics. The similarity between PYTHIA and the experimental data offers a promising path forward to understand the mechanism in QCD driving the observed evolution in more detail.





PHENIX  $\pi^0$ - $h^+$  and  $\gamma$ - $h^+$   $p_{\text{out}}$  distributions for  $|\eta| < 0.35$  and  $0.7 < p_T^{\text{assoc}} < 10$  GeV/c. The solid lines represent the PYTHIA Perugia0 simulation, and the dashed lines represent the linear fit to the data.



PHENIX  $\pi^0$ - $h^+$  and  $\gamma$ - $h^+$   $p_{\text{out}}$  distributions for  $|\eta| < 0.35$  and  $0.7 < p_T^{\text{assoc}} < 10$  GeV/c. The solid lines represent the PYTHIA Perugia0 simulation, and the dashed lines represent the linear fit to the data.

## ACKNOWLEDGMENTS

We thank the staff of the Collider-Accelerator and Physics Departments at Brookhaven National Laboratory and the staff of the other PHENIX participating institutions for their vital contributions. We also thank T.C. Rogers, J.C. Collins, and L. Lönnblad for valuable discussions regarding the interpretation of these results, as well as T. Kaufmann for providing several pQCD calculations. We acknowledge support from the Office of Nuclear Physics in the Office of Science of the Department of Energy, the National Science Foundation, Abilene Christian University Research Council, Research Foundation of SUNY, and Dean of the College of Arts and Sciences, Vanderbilt University (U.S.A), Ministry of Education, Culture, Sports, Science, and Technology and the Japan Society for the Promotion of Science (Japan), Conselho Nacional de Desenvolvimento Científico e Tecnológico and Fundação de Amparo à Pesquisa do Estado de São Paulo (Brazil), Natural Science Foundation of China (People's Republic of China), Croatian Science Foundation and Ministry of Science, Education, and Sports (Croatia), Ministry of Education, Youth and Sports (Czech Republic), Centre National

de la Recherche Scientifique, Commissariat à l'Énergie Atomique, and Institut National de Physique Nucléaire et de Physique des Particules (France), Bundesministerium für Bildung und Forschung, Deutscher Akademischer Austausch Dienst, and Alexander von Humboldt Stiftung (Germany), National Science Fund, OTKA, Károly Róbert University College, and the Ch. Simonyi Fund (Hungary), Department of Atomic Energy and Department of Science and Technology (India), Israel Sci-

ence Foundation (Israel), Basic Science Research Program through NRF of the Ministry of Education (Korea), Physics Department, Lahore University of Management Sciences (Pakistan), Ministry of Education and Science, Russian Academy of Sciences, Federal Agency of Atomic Energy (Russia), VR and Wallenberg Foundation (Sweden), the U.S. Civilian Research and Development Foundation for the Independent States of the Former Soviet Union, the Hungarian American Enterprise Scholarship Fund, and the US-Israel Binational Science Foundation.

JGHEP	193,80				
JGHEP	194,00				
JGHEP	250,9				
JGHEP	41,80				
JGHEP	43,00				
JGHEP	461,90				
JGHEP		Foundations of perturbative QCD			
JGHEP	85,00				
JGHEP	83,00				
JGHEP	110,00				
JGHEP		<i>et al.</i>			
JGHEP	94,00				
JGHEP	744,00				
JGHEP		<i>et al.</i>			
JGHEP			$p+p \rightarrow$		
JGHEP	102,0				
JGHEP		<i>et al.</i>			
JGHEP	37,00				
JGHEP		<i>et al.</i>			
JGHEP	D 39,00				
JGHEP		<i>et al.</i>			
JGHEP	116,00		$p^+ + p \rightarrow$		
JGHEP					
JGHEP					
JGHEP	107,00				$^3\text{H}$
JGHEP		<i>et al.</i>			
JGHEP	105,00				
JGHEP		<i>et al.</i>			
JGHEP			$e^+e^- \rightarrow$		96,
JGHEP		<i>et al.</i>			
JGHEP			$+e^- \rightarrow$		
JGHEP	D 90,00				
JGHEP		<i>et al.</i>			
JGHEP	693,10				
JGHEP		<i>et al.</i>			
JGHEP			$\sqrt{s} \rightarrow$		$\eta$ in $p^+$
JGHEP	90,00				
JGHEP		<i>et al.</i>			
JGHEP					$\sqrt{s} \rightarrow$
JGHEP	92,00				
JGHEP		<i>et al.</i>			
JGHEP			$p+p \rightarrow$		$\sqrt{s} \rightarrow$
JGHEP	101,00				
JGHEP	656,00				
JGHEP					
JGHEP					530,00
JGHEP	536,00				
JGHEP					
JGHEP					81,00
JGHEP					
JGHEP	47,00				
JGHEP					$k_T$ in $\text{is}$
JGHEP					75,



112,0  
 83,0  
 et al. 1981  
 $k_T$   
 $pp$   
 $\sqrt{s} = 1.6$   
 85,0  
 et al. 1981

102,

90,  
 $\sqrt{s} = 1.6$   
 88,0  
 82,0  
 et al. 1981  
 $e^+e^-$   
 $pp$   
 $\sqrt{s} = 1.6$   
 86,